

DEEPMIR: A DEEP convolutional neural network for differential detection of cerebral Microbleeds and IRon deposits in MRI

Tanweer Rashid^{1,8}, Ahmed Abdulkadir^{1,2}, Ilya M. Nasrallah^{1,3}, Jeffrey B. Ware³, Pascal Spincemaille⁴, J. Rafael Romero⁵, R. Nick Bryan^{3,6}, Susan R. Heckbert⁷, Mohamad Habes^{1,8}

1 Center for Biomedical Image Computing and Analytics (CBICA), University of Pennsylvania, Philadelphia, PA, USA

2 University Hospital of Old Age Psychiatry and Psychotherapy, University of Bern, Bern, Switzerland

3 Department of Radiology, Hospital of University of Pennsylvania, Perelman School of Medicine of the University of Pennsylvania, Philadelphia, PA, USA

4 Department of Radiology, Weill Cornell Medical College, New York, NY, USA

5 Department of Neurology, School of Medicine, Boston University, Boston, MA, USA

6 Department of Diagnostic Medicine, Dell Medical School, University of Texas at Austin, Austin, TX, USA

7 Department of Epidemiology and Cardiovascular Health Research Unit, University of Washington, Seattle, WA, USA

8 Neuroimage Analytics Laboratory (NAL) and the Biggs Institute Neuroimaging Core (BINC), Glenn Biggs Institute for neurodegenerative disorders, University of Texas Health Science Center at San Antonio (UTHSCSA), San Antonio, USA

Corresponding author: habes@uthscsa.edu

Abstract:

Background: Lobar cerebral microbleeds (CMBs) and localized non-hemorrhage iron deposits in the basal ganglia have been associated with brain aging, vascular disease and neurodegenerative disorders. Recent advances using quantitative susceptibility mapping (QSM) make it possible to differentiate iron content from mineralization in-vivo using magnetic resonance imaging (MRI). However, automated detection of such lesions is still challenging, making quantification in large cohort bases studies rather limited.

Purpose: Development of a fully automated method using deep learning for detecting CMBs and non-hemorrhage basal ganglia iron deposits using multimodal MRI.

Materials and Methods: We included a convenience sample of 24 participants from the MESA cohort and used T2-weighted images, susceptibility weighted imaging (SWI), and QSM to segment the lesions. We developed a protocol for simultaneous manual annotation of CMBs and non-hemorrhage iron deposits in the basal ganglia, which resulted in defining the gold standard. This gold standard was then used to train a deep convolution neural network (CNN) model. Specifically, we adapted the U-Net model with a higher number of resolution layers to be able to detect small lesions such as CMBs from standard resolution MRI which are used in cohort-based studies. The detection performance was then evaluated using the cross-validation principle in order to ensure generalization of the results.

Results: With multi-class CNN models, we achieved an average sensitivity and precision of about 0.8 and 0.6, respectively for detecting CMBs. The same framework detected non-hemorrhage iron deposits reaching an average sensitivity and precision of about 0.8.

Conclusions: Our results showed that deep learning could automate the detection of small vessel disease lesions and including multimodal MR data such as QSM can improve the detection of CMB and non-hemorrhage iron deposits.

Keywords: cerebral microbleeds, iron deposits, brain lesions, deep learning

Word count: 5163

1 Introduction

The aging brain is subject to various irreversible changes, some driven by the aging process itself and others that are associated with various pathologies including vascular disease and neurodegeneration (1-4). Magnetic resonance imaging (MRI) using sequences sensitive to magnetic susceptibility can detect the focal accumulations of iron that are frequently observed in elderly populations, including in cerebral microbleeds (CMBs) and non-hemorrhage iron deposits in the basal ganglia. CMBs are small hemorrhages that can occur anywhere in the brain, largely sporadically (5). The presence of lobar CMBs is also a marker for cerebral amyloid angiopathy (6-8). On the other hand, non-hemorrhage iron deposits tend to be more localized in the deep structures of the brain, particularly in the basal ganglia. While some increase in iron concentration in the basal ganglia is expected in healthy aging (9), excessive accumulation of iron has been associated with neurodegenerative disorders (10-12).

CMB confer important clinical information, so manual quantification/rating systems such as the Microbleed Anatomical Rating Scale (MARS) (13) and Brain Observer MicroBleed Scale (BOMBS) (14) were developed for structured assessment of lesion load of CMBs. These rating scales represent the lesion load in tables listing the number of CMBs in seven (in BOMBS) to thirteen (in MARS) bilateral regions, with separate counts for smaller (< 5 mm) and larger lesions in BOMBS. They include the assignment of a level of confidence (certain/uncertain) to each detected potential microbleed. Manual annotation of CMBs in the images would retain more information about the spatial distribution and the size of individual CMBs compared to these rating systems but would be even more labor intensive.

CMBs and non-hemorrhage iron deposits both have a similar appearance in several MRI modalities (15). The contrast to surrounding tissue is particularly strong in T2* gradient-recalled echo (GRE) and susceptibility-weighted imaging (SWI) due to strong paramagnetic effects of iron present in both types of lesions. Of these two modalities, SWI was more sensitive than T2* GRE for detecting CMBs (16, 17). In the images acquired with these modalities, CMBs appear as small rounded or ellipsoidal hypointense regions with a diameter of ten millimeters or less (6, 15, 18). Non-hemorrhage iron deposits in the basal ganglia generally do not conform to any specific shapes and are observed to be larger in size than CMBs. One useful distinction between the two, however, is that typical focal iron deposits are mainly located in the gray matter of the basal ganglia, particularly the globus pallidus, whereas CMBs can occur anywhere, and overall, infrequently in the globus pallidus (15). Because hypo-intensities in SWI are not specific to CMBs and non-hemorrhage iron deposits, images with other tissue contrasts are required in order to identify other lesion types that can have similar low signal on SWI, such as enlarged perivascular space (EPVS), infarcts, or calcification (5, 13, 14). The specificity for CMB detection can be increased by post-processing SWI-magnitude and phase data to derive maps of tissue susceptibility, known as quantitative susceptibility mapping (QSM) (19, 20). QSM allows magnetic susceptibility from paramagnetic materials to be differentiated from that deriving from diamagnetic materials, and therefore is particularly useful for distinguishing non-hemorrhage iron deposits from calcifications (21, 22). Studies have shown SWI and

QSM to be useful for deriving metrics for CMBs and iron deposits (21, 23). Panels A and B in Figure 1 show examples of CMBs and non-hemorrhage iron deposits on SWI, QSM and T2 MRI. Mimics such as enlarged perivascular spaces (EPVS) and calcifications have an appearance on SWI that is similar to that of CMBs. EPVS can be easily differentiated from CMBs using T2-weighted images where they appear hyper-intense. Panel B in Figure 1 shows an example of an EPVS on SWI, QSM and T2 MRI. Calcifications are distinguishable from CMBs using QSM (21) or, sometimes, when viewed on CT.

The location, number, and size of the two types of iron-containing lesions vary substantially across individuals. Thus, advancing the understanding of the role and relations of these lesions with various brain pathologies requires large samples to sufficiently cover the variability in population and across disorders. Automatic processing may reduce otherwise necessary manual annotation work and thus facilitate research in large cohort samples. We developed robust and fully automated deep learning-based method to detect CMBs and non-hemorrhage iron deposits in a cohort without extensive apparent brain tissue damage and with a low load of CMBs and non-hemorrhage basal ganglia iron deposits. We experimented with both single class and multiclass models using multiple MR modalities. Our experiments show that using multi-modal MRI improves the accuracy of detection.

2 Materials and Methods

2.1 MRI Acquisition and Pre-Processing

The Multi-Ethnic Study of Atherosclerosis (MESA) Exam 6 Atrial Fibrillation Ancillary Study’s brain MRI protocol included T1-weighted, T2-weighted and a QSM susceptibility-weighted sequence with 4 SWI at different, equally spaced echo times. SWI is a high-resolution, 3D imaging sequence where the image contrast is enhanced by combining magnitude and phase image data (24, 25). The scans were acquired at 6 sites using the same acquisition parameters. All scans were performed on Siemens MR scanners (2 Skyra with 20 channel head coil and 4 Prisma Fit with 32 channel head coil) at a static magnetic field strength of 3 Tesla and identical imaging sequence parameters, as shown in Table 1.

Note that multiple SWI phase and magnitude images were acquired with varying echo times (Table 1). SWI data were generated following the proposed method of Haacke et al (24, 26). A phase mask was generated from the phase images using a high-pass filter of size 64 x 64 in order to remove artifacts. The SWI was generated by multiplying the magnitude image with the phase mask. For creation of the reference annotation and machine-based inference, only the SWI image with the shortest echo time (TE=7.5 ms) was used as this would potentially result in a smaller number of false positives compared to a longer TE (27).

The T1 and T2 images underwent N4 bias correction (28) with default parameters using the implementation in the Advanced Normalization Tools¹ (ANTs) suite and were rigidly registered to the participants’ SWI

¹ <http://stnava.github.io/ANTs/>

image using FSL's FLIRT² (29-31). Anatomical parcellation and brain masks were generated with a multi-atlas segmentation method using the bias corrected T1 images (32). These brain masks were used in the generation of the QSM images. QSM maps required also the entire multi-echo SWI dataset using the Morphology Enabled Dipole Inversion (MEDI)³ method (20, 33) implemented in MATLAB.

2.2 Manual Annotation

Manual annotation was performed according to a custom protocol developed with the focus on highly specific differential detection of CMBs and non-hemorrhage iron deposits based on multiple modalities. The detailed protocol is reported in Supplementary Materials 1, S1.1, and a flowchart of the manual annotation process is shown in Figure S 1.

2.3 Study Participants

We included imaging data from participants in the MESA Exam 6 Atrial Fibrillation Ancillary Study (34-36). A subset of the MESA cohort participated in an ancillary study of cardiac arrhythmias and brain imaging during the 2016-2018 exam (Exam 6) (37). From among 1061 participants who underwent MR brain scans, a convenience sample of 34 scans was selected based on prior visual identification of possible CMBs by two experienced readers (IMN and TR). These 34 participants are not representative of the MESA cohort in terms of prevalence of CMBs and non-hemorrhage iron deposits, and additional participants in the MESA cohort likely have CMBs and/or non-hemorrhage iron deposits. A total of 10 participants' scans were excluded due to poor image quality (n=4) and presence of distortions/artefacts or motion-related effects (n=6). The demographics summary and lesion loads for the 24 included participants are presented in Table 2. Of these 24 participants, there were 13 males and 11 females with age range 65-94 years. Based on the expert annotation of these 24 participants, 4 participants had no microbleeds, 13 participants had 1 or 2 microbleeds (with average size of 10.85 mm³), 6 participants had between 3 and 8 microbleeds (with average size of 10.21 mm³) and 1 participant had more than 100 microbleeds (with average size of 4.76 mm³). In certain circumstances, the participant with more than 100 microbleeds may be considered an outlier in terms of the number of CMBs. An examination of this is presented in Supplementary Materials 4, section S 4.1. Of the 24 participants, 5 participants did not have any voxels labeled as non-hemorrhage iron deposits and the remaining had between 2 (each having a single voxel or 1.5 mm³) and 13 lesions (one participant had 4 non-hemorrhage iron deposit lesions with a total of 326 voxels or 489 mm³) labeled as non-hemorrhage iron deposits in the basal ganglia.

The distribution of CMBs and iron deposits pooled over all participants is illustrated in Figure 2. The average size (\pm SEM, or standard error of the mean) of CMB lesions in this sample was 6.27 ± 0.51 mm³ (4.18 ± 0.34 voxels). Among the 20 participants with CMB, 70% (n =14) had two or fewer CMBs, 25% (n = 5) had between three and eight CMBs, and the remaining participant had 120 CMBs. The average size of non-hemorrhage iron deposit labels (\pm SEM) was 26.15 ± 4.76 mm³ (17.43 ± 3.17 voxels). Approximately

² <https://fsl.fmrib.ox.ac.uk>

³ <http://weill.cornell.edu/mri/pages/qsm.html>

21% ($n = 5$) had no discernable basal ganglia non-hemorrhage iron deposits and half ($n = 12$) had fewer than 100 voxels (150 mm^3) labeled as non-hemorrhage iron deposits. The remaining 29% ($n = 7$) had more than 100 voxels labeled as non-hemorrhage iron deposits.

2.4 Method Overview for Automated Processing

We developed a deep learning framework for automatic segmentation of CMBs and non-hemorrhage iron deposits based on the U-Net (38, 39), a widely used deep learning architecture for image segmentation. Our architecture, however, employed padded instead of unpadded convolutions and operated on six instead of five spatial resolutions, and was used for both single class and multiclass segmentation experiments. The detailed description of our implementation can be found in Supplementary Materials 2, S 2.1. The overall system pipeline is shown in Figure 3. After the initial step of co-registration the MR volumes were preprocessed to have zero mean and unit variance, as detailed in Supplementary Section 3 (S 3.1). The normalized MR volumes were then sliced along the z -axis (axial slices) and padded with zeros to obtain 2D slices with 256×256 voxels. We evaluated the performance considering the leave-one-out cross-validation for the 24 participants listed in Table 2 to ensure generalization of results. In each fold, a single participant's data was kept separate for testing (test dataset), and the MR data and labels from the remaining 23 participants were randomly split into training dataset (75%, consisting of 17 participants) and validation datasets (25%, consisting of 6 participants). Both training and validation datasets were augmented to improve the robustness of the deep learning models. Details regarding dataset augmentation is reported in Supplementary Materials 3 (S 3.2). The training dataset was used to train the model for a single epoch, after which the validation dataset was used to compute a commonly used evaluation metric known as intersection-over-union (IoU) which quantifies the amount of overlap between the predicted and groundtruth segmentations. Each model was trained for a maximum of 30 epochs, and a "best" model was determined as the model with the maximum IoU. This "best" model was then used to predict the labels of the test dataset. The set of predictions used for evaluating model performance thus consisted of 24 segmentation masks that were predicted with 24 different models with no overlap between training, validation and testing datasets. These evaluations were for single class and multiclass experiments. For both single class and multiclass experiments, four permutations of MR modalities were considered: (1) SWI only, (2) SWI and QSM, (3) SWI and T2, and (4) SWI, QSM and T2.

For single class experiments, the models were trained and evaluated for (1) CMBs only, (2) non-hemorrhage iron deposits only, and (3) CMBs \cup iron deposits (both having the same label). For multiclass experiments, both CMBs and iron deposits had separate labels, and were segmented simultaneously. For multi-class segmentations, a larger number of augmentations were used than for single class segmentations.

2.5 Evaluation of Performance

We evaluated the performance in terms of rate of detected/missed CMBs and non-hemorrhage iron deposit lesions. For each participant, the number of true positives (TP), false positives (FP) and false negatives (FN) was counted as follows: first, a connected-component filter with 3D connectivity was applied to both

the predicted segmentation and the reference segmentation in order to identify clusters of voxels. Next, the centroid of each component in both the predicted segmentation and reference was computed. TP, FP and FN were determined on whether the Euclidean distance between a predicted component and a reference component was below a specified tolerance. A tolerance of 3 was used for evaluating CMBs and a tolerance of 5 was used for evaluating non-hemorrhage iron deposits since iron deposits have a more dispersed pattern than CMBs which are spherical in shape. The sensitivity (or true positive rate) was computed as the ratio of TP and number of lesions in the ground truth (TP + FN) for each participant. The precision (or positive predictive value) was computed as the ratio of TP and the number lesions in the predicted mask (TP + FP). When the true negative (TN) is available, the typical measure of performance is the accuracy, determined by $(TP + TN) / (TP + TN + FP + FN)$. In our application, the true negative (TN) is difficult to estimate because the true negative encompasses all regions of the volume that are not CMBs or non-hemorrhage iron deposits.

To evaluate the performance of each model, we report the average sensitivity across all participants and average precision across all participants, as well as a combined metric (magnitude accuracy) computed as $\sqrt{AvgSensitivity^2 + AvgPrecision^2}$.

2.6 Statistical Analysis

Due to small sample size and potential non-uniform distribution of the models' sensitivity, precision and magnitude accuracy, we utilized the non-parametric two-tailed Wilcoxon rank sum test to check for difference between the performance of the various models. In all single class and multiclass experimental evaluations, the model trained with only SWI is considered as the baseline model for comparison. Statistical significance was considered at a $p < 0.05$. All statistical analysis was performed using MATLAB R2017b.

3 Results

3.1 Single Class Model

In this evaluation, only a single class of lesions was considered at a time: either CMBs alone, non-hemorrhage iron deposits alone, or lesions consisting of either type without making a distinction between types. The average sensitivity, average precision, average magnitude accuracy and false positives per participant for experiments based on the single class models are reported in Table 3, along with their respective standard errors of the mean (SEM) and the lower and upper bounds based on 95% confidence interval. For detecting only CMBs, the best model was the one trained with SWI and QSM, having an average of 0.88 and precision 0.40, with a combined magnitude accuracy of 1.09 and 4.33 false positives (FPs) per participant. The model trained with SWI, QSM and T2 also resulted in comparable performance in terms of magnitude accuracy (1.08) having an average sensitivity and precision of 0.87 and 0.50, respectively, but produced the fewest FPs per participant (2.79). A comparison against the baseline model

(the model trained with only SWI) revealed that the average magnitude accuracy of the model trained with SWI and QSM was better ($p = 0.014$) and the average precision and magnitude accuracy for the model trained with all modalities was yielding the better results ($p = 0.012$ and $p = 0.009$, respectively).

For the task of detecting iron deposits only, the best model was the one trained with SWI, QSM and T2 having an average sensitivity and precision of 0.81 and 0.62, respectively, with a magnitude accuracy of 1.11 and 2.50 FPs per participant. Similar to detecting CMBs only, we noted that the model trained with SWI and QSM also had a similar performance in terms of magnitude accuracy (1.09), with average sensitivity and precision of 0.77 and 0.60, respectively and 2.71 FPs per participant.

A joint scatterplot of the sensitivity and precision for all single class model experiments involving CMBs only or non-hemorrhage iron deposits only is shown in Figure 4. In the subplots of this figure, the round points represent individual participants' sensitivity and precision, and the X marker represents the average of sensitivity and precision of the experiment. The coordinates of the X marker, i.e. the average sensitivity and precision of the experiment is shown in the legend located in the upper left corner of each subplot. The histogram of the magnitude accuracies for the single class experiments is shown in Figure 6 (top row).

Another experiment was performed where the combined CMB and iron deposit labels were evaluated. These results are described in Supplementary Section 3.3.

Panels C and D of Figure 1 shows the segmentation of CMB and iron deposits of the brain slices shown in Figure 1, Panels A and B, respectively. In these figures, the segmentation map is produced by the model trained with the combined CMB and iron deposit reference annotation. Figure 7 (Panel A) shows the segmentation result using a model that was trained using SWI, QSM and T2 based on combined reference annotation. On this axial slice of this figure, both an enlarged perivascular space (yellow arrow) and a small microbleed (a single voxel in size) are present. In this case, the model correctly rejected the EPVS as a mimic while correctly segmenting the CMB.

3.2 Multi-class Model

In this analysis, CMBs and non-hemorrhage iron deposits were treated as individual types of lesions and predicted/evaluated simultaneously. The corresponding average sensitivity, average precision, average magnitude accuracy and false positives (FP) per participant are reported in Table 3, along with their respective standard errors of the mean (SEM) and the lower and upper bounds based on 95% confidence interval. The model trained with SWI and QSM had the best performance. For CMBs, the highest magnitude accuracy was 1.15 with an average sensitivity and precision of 0.84 and 0.59, respectively with 1.83 FPs per participant. As observed with the single class experiments, the next best performance in terms of magnitude accuracy (1.07) was obtained with the model trained with SWI, QSM and T2 having an average sensitivity and precision of 0.89 and 0.49, respectively with the next lowest FPs per participant of 2.08. When compared to the baseline model trained with only SWI, the precision and magnitude accuracy for the model trained with SWI and QSM was found to be better ($p = 0.045$ and $p =$

0.006, respectively). The magnitude accuracy of the model trained with SWI, QSM and T2 was also found to be better ($p = 0.022$).

For detecting iron deposits with the multi-class models, the best performing model was the one trained with SWI and QSM having an average sensitivity, precision and magnitude accuracy of 0.75, 0.75 and 1.20, respectively with 1.29 FPs per participant. The next best performing model in terms of magnitude accuracy (1.17) was the model trained with SWI, QSM and T2 having an average sensitivity and precision of 0.81 and 0.64, respectively with 1.88 FPs per participant.

A joint scatterplot of the sensitivity and precision for the multiclass model experiments are shown in Figure 5. In the subplots of this figure, the round points represent individual participants' sensitivity and precision, and the X marker represents the average of sensitivity and precision of the experiment. The coordinates of the X marker, i.e. the average sensitivity and precision of the experiment is shown in the legend located in the upper left corner of each subplot. The histogram of the magnitude accuracies for the multiclass experiments is shown in Figure 6 (bottom row). Figure 7, Panel B shows an example of non-hemorrhage iron deposit segmentation using a multiclass model trained with SWI, QSM and T2. In this figure, there is a small mineralization deposit present in the basal ganglia (marked with blue arrow) appearing hypo-intense on QSM. The model was able to correctly reject the mineralization as a mimic while correctly segmenting the surrounding iron deposits.

An example of the multi-class segmentation with both CMB and non-hemorrhage iron deposits is shown in Figure 8.

Finally, removing outlier data using a Beta distribution fit resulting in the removal of a single participant with >100 CMBs from our sample in a sensitivity analysis, showed largely similar performance (Supplementary Materials 4, S 4.2).

4 Discussion

In this work, we developed and implemented a deep learning framework and trained it for the segmentation of CMBs and non-hemorrhage iron deposits using multi-modal MRI. The highest accuracy for automated quantification of CMB and non-hemorrhage iron deposits in the brain was achieved when multiple modalities were used. We made use of a rather novel advanced imaging contrast, QSM, that helped distinguish iron content from mineralization (in this, possibly calcification), as shown in Panel B of Figure 7. Although calcification and calcium deposits can be clearly visible in computed tomography (CT) images (40, 41) our proposed imaging and analysis pipeline is based solely on MRI and thus does not require the use of ionizing radiation. We experimented with several permutations of the available MR modalities, with SWI being utilized in all cases. When considering the models trained only SWI as a baseline, statistical analysis revealed that using QSM confers significant improvement in the precision and overall magnitude

accuracy for detecting CMBs, including a reduction in the number of false positives per participant. Our method can be integrated in pipelines for automated reading of large-scale cohort studies.

Automatic detection of CMBs and iron deposits is a challenging task that requires specialized imaging sequences and benefits from post-processing of multi-time echo images. Most lesions were very small, infrequent and appeared throughout the brain, and shared their intensity profile with other types of lesions such as EPVSs and calcifications. Thus, even when QSM is available, the detection task could be inherently more complicated than the task of segmenting other larger targets such as white matter hyperintensities and anatomical regions. White matter hyperintensities are usually delineated on a single image modality and tend to be present in greater volume than CMBs and non-hemorrhage iron deposits (42). Anatomical regions are also mostly delineated on a single modality and are substantially larger as well (43).

There have been several attempts to detect CMBs using traditional machine learning-based methods. The typical approach is to pass the raw data through a feature extraction stage which outputs a set of feature vectors from which the selected machine learning algorithm determines the optimal decision boundary. For example, radial symmetry transforms were used with 3T SWI (44) and 7T dual-echo T2* images (45), fast radial symmetry transforms were used on 3T minimum intensity projection SWI (46), and 3D hierarchical feature extraction via a stacked convolutional Independent Subspace Analysis network were used on 3T SWI (47). These studies reported an average sensitivity ranging between 71.2% to 89.4%. Apart from these supervised machine learning-based methods, one study (48) utilized a generative latent tissue class model based on (49), with CMBs being a separate *atypical* class to segment CMBs on 1.5T T2*-weighted images.

Chen et al. (50) used fast radial symmetry transforms to identify candidate CMBs on 7T SWI, which was followed by a 3D convolution network with residual connections, achieving a sensitivity of 95% in 12 test subjects. The method by Liu et al. (51) used 3D fast radial symmetry transform on permutations of SWI, SWI-magnitude, SWI-phase and QSM images (from 1.5T and 3T scanners) as the initial stage, followed by 3D convolution network with residual connections, achieving a sensitivity of 95.8% and precision of 70.9%. An approach to analyze 3T SWI data using two 3D deep convolutional neural networks was presented by Dou et al. (52) and achieved a sensitivity of 93.2% and precision of 44.3%.

Our approach has several advantages over the current state of the art in the detection of CMBs. First, we employ end-to-end learning by using a single model (network) rather than multiple stages (50-52), and our approach has sensitivity and precision comparable to existing methods. This experimental design allows for greater flexibility, for example in retraining with different or larger data sets, adding additional class labels (such as EPVSs), or using different modalities because the principle of training is consistent and does not involve feature engineering or implementation of new neural network architectures. The maximum performance of the network is not limited by the choice of hand-engineered features. Second, we trained with different sets of input imaging modalities. Combinations of imaging modalities allowed our models to reject mimics such as EPVSs and calcifications without explicit provisions (as shown in Figure 7, Panels A and B). The models in (50, 52) used SWI only and may not be capable of recognizing and rejecting

mimics. The model in (51) utilizes SWI-phase and magnitude images along with QSM, but ignored voxels in the basal ganglia using an atlas. Third, we investigated the performance of the same CNN architecture in different tasks that either involved the detection of a single type of lesions, the union of both labels, or the simultaneous labelling of both labels with different classes (Figure 8).

One of the major challenges was the small size of the lesions and their potential presence throughout the brain. The average size of four voxels (or 6 mm^3) per CMB together with the generally low lesion burden of the study participants resulted in including only two CMB lesions/4 voxels on average per participant, resulting in a higher weight of a single lesion or error in the evaluation. In other words, missing a single lesion would result in a drop of sensitivity from one to 0.5 and a single false positive for a given participant would result in drop of that participant's precision from one to 0.5 or 0.66. Similarly, a small number of false positives, in absolute terms, can lower the average precision substantially. In general, our models over-segmented the data. In all experiments using the aforementioned combinations of available imaging modalities, most of the lesions were detected and the average sensitivity was consistently above 0.7. The precision reached a value of 0.62 for only iron deposits and 0.50 for only CMBs when all modalities were included for training, indicating that about half of the objects identified as lesions were falsely characterized. In the case of multi-class segmentation, the overall sensitivity and precision increased.

Notably the sample used to train the model is a convenience sample of relatively healthy participants (i.e. without an overwhelming prevalence of CMBs) from the MESA cohort. Given the low number of lesions on average, our method achieved sensitivities that are comparable to other published studies on CMB segmentation/detection and including more samples with more lesions would likely improve the precision. In general, most studies incorporating automated methods for large-scale abnormality detection or brain region segmentation incorporate a segmentation quality control step that could result in corrections or exclusions (1, 53, 54). Thanks to the flexibility of our method, using a larger training sample size or additional modalities is possible without modification to the architecture or optimization of hyperparameters.

T2* GRE images and SWI acquired with different echo times and different magnetic field strengths vary in image quality as well as sensitivity and specificity with respect to the detection of CMBs and iron deposits (16, 27, 55). With the employed model, empirical evaluation of the effects of multiple echo times on the detection accuracy can readily be implemented. The flexibility of the framework goes beyond sample size and input data. In this study, we included two clinically relevant labels, but alternative definitions of the lesion types and even additional classes such as EPVSs and calcification can be included, given the availability of reference annotations. The varying levels of confidence in individual segmentations could be incorporated in the training by using the relative frequency from multiple raters as target. This could account for the ambiguity and conflicting classifications across raters.

As mentioned previously, most participants had few CMBs. In clinical terms, a larger number of CMBs is more likely to be clinically relevant. The automated detection method presented here was trained and

evaluated on a relatively small population, and outputs the number of lesions and lesion segmentation maps for each participant. The next step would be to rigorously test and evaluate the proposed model on a larger sample size to ensure viable sensitivity, precision and accuracy, before applying this method to a large cohort in order to determine the prevalence of lesions in the population. In theory, an adequately trained model can be used as a screening tool to flag participants having a high lesion load while ignoring participants with a low lesion load. The method presented here can also be potentially used for screening and generating an initial segmentation of lesions, which can be then be fine-tuned by a human expert to reduce false positives. Since the deep learning models used here outputs a segmentation map, the effort on part of the expert would be significantly reduced in terms of locating the lesions.

The main limitation to this study is the relatively small number of participant data used for training and model evaluation. To achieve leave-one-out cross-validation with this small sample size of 24 participants, one participant's data was reserved for testing, while 6 participants' data was used for model validation and the remaining (17 datasets) were used for training during a single cross-validation fold. For our purposes, this ratio of validation to training data (25:75) is reasonable because we want to ensure that a maximal amount of the available data is used in model training, while at the same time, a sufficient amount is reserved for within-training validation. During each cross-validation fold the testing, training and validation data were completely non-overlapping to ensure that data leakage did not occur. Additionally, a new model is trained, validated and finally tested for each cross-validation fold to avoid any recursive effects. The use of a similar sample size for training and evaluation is not completely unprecedented: for example, Barnes et al. (56) used a total of 6 subjects, Kuijf et al. (45) used 18 subjects, Seghier et al. (48) used 30 subjects and Fazlollahi et al. (57) used 16 subjects with CMBs. However, a lower sample size obviously reduces the statistical power of the study. Even though the use of QSM seems to reduce the number of false positives per participant, it is not clear if using a specific permutation of MR modalities is statistically significant over other permutations of MR modalities. Nor was it possible to conclusively determine the effects on sensitivity, precision and magnitude accuracy when including or excluding a potential outlier participant.

This study tackled the challenging task of detecting small CMBs and non-hemorrhage iron deposits and at the same time provides excellent capability for further extensions and additional development through the use of alternative imaging sequences, larger data sets, or inclusion of multiple reference annotations.

5 Acknowledgements

This research was supported by contracts 75N92020D00001, HHSN268201500003I, N01-HC-95159, 75N92020D00005, N01-HC-95160, 75N92020D00002, N01-HC-95161, 75N92020D00003, N01-HC-95162, 75N92020D00006, N01-HC-95163, 75N92020D00004, N01-HC-95164, 75N92020D00007, N01-HC-95165, N01-HC-95166, N01-HC-95167, N01-HC-95168 and N01-HC-95169 and grant HL127659 from the National Heart, Lung, and Blood Institute, and by grants UL1-TR-000040, UL1-TR-001079, and

UL1-TR-001420 from the National Center for Advancing Translational Sciences (NCATS). The content is solely the responsibility of the authors and does not necessarily represent the official views of the National Institutes of Health. The authors thank the other investigators, the staff, and the participants of the MESA study for their valuable contributions. A full list of participating MESA investigators and institutions can be found at <http://www.mesa-nhlbi.org>.

6 References

1. Habes M, Erus G, Toledo JB, Zhang T, Bryan N, Launer LJ, et al. White matter hyperintensities and imaging patterns of brain ageing in the general population. *Brain*. 2016;139(4):1164-79.
2. DeBette S, Beiser A, DeCarli C, Au R, Himali JJ, Kelly-Hayes M, et al. Association of MRI markers of vascular brain injury with incident stroke, mild cognitive impairment, dementia, and mortality: the Framingham Offspring Study. *Stroke*. 2010;41(4):600-6.
3. Ge Y, Grossman RI, Babb JS, Rabin ML, Mannon LJ, Kolson DL. Age-related total gray matter and white matter changes in normal adult brain. Part I: volumetric MR imaging analysis. *American journal of neuroradiology*. 2002;23(8):1327-33.
4. Scahill RI, Frost C, Jenkins R, Whitwell JL, Rossor MN, Fox NC. A longitudinal study of brain volume changes in normal aging using serial registered magnetic resonance imaging. *Archives of neurology*. 2003;60(7):989-94.
5. Charidimou A, Jäger HR, Werring DJ. Cerebral microbleed detection and mapping: principles, methodological aspects and rationale in vascular dementia. *Experimental gerontology*. 2012;47(11):843-52.
6. Haller S, Vernooij MW, Kuijter JP, Larsson E-M, Jäger HR, Barkhof F. Cerebral microbleeds: imaging and clinical significance. *Radiology*. 2018;287(1):11-28.
7. Vernooij M, van der Lugt A, Ikram MA, Wielopolski P, Niessen W, Hofman A, et al. Prevalence and risk factors of cerebral microbleeds: the Rotterdam Scan Study. *Neurology*. 2008;70(14):1208-14.
8. Cordonnier C, van der Flier WM. Brain microbleeds and Alzheimer's disease: innocent observation or key player? *Brain*. 2011;134(2):335-44.
9. Acosta-Cabronero J, Betts MJ, Cardenas-Blanco A, Yang S, Nestor PJ. In vivo MRI mapping of brain iron deposition across the adult lifespan. *Journal of Neuroscience*. 2016;36(2):364-74.
10. Ward RJ, Zucca FA, Duyn JH, Crichton RR, Zecca L. The role of iron in brain ageing and neurodegenerative disorders. *The Lancet Neurology*. 2014;13(10):1045-60.
11. Bartzokis G, Tishler TA, Lu PH, Villablanca P, Altshuler LL, Carter M, et al. Brain ferritin iron may influence age- and gender-related risks of neurodegeneration. *Neurobiology of aging*. 2007;28(3):414-23.
12. House MJ, Pierre TS, Foster J, Martins R, Clarnette R. Quantitative MR imaging R2 relaxometry in elderly participants reporting memory loss. *American Journal of Neuroradiology*. 2006;27(2):430-9.
13. Gregoire S, Chaudhary U, Brown M, Yousry T, Kallis C, Jäger H, et al. The Microbleed Anatomical Rating Scale (MARS): reliability of a tool to map brain microbleeds. *Neurology*. 2009;73(21):1759-66.
14. Cordonnier C, Potter GM, Jackson CA, Doubal F, Keir S, Sudlow CL, et al. Improving interrater agreement about brain microbleeds: development of the Brain Observer MicroBleed Scale (BOMBS). *Stroke*. 2009;40(1):94-9.
15. Greenberg SM, Vernooij MW, Cordonnier C, Viswanathan A, Salman RA-S, Warach S, et al. Cerebral microbleeds: a guide to detection and interpretation. *The Lancet Neurology*. 2009;8(2):165-74.

16. Nandigam R, Viswanathan A, Delgado P, Skehan M, Smith E, Rosand J, et al. MR imaging detection of cerebral microbleeds: effect of susceptibility-weighted imaging, section thickness, and field strength. *American Journal of Neuroradiology*. 2009;30(2):338-43.
17. Ayaz M, Boikov AS, Haacke EM, Kido DK, Kirsch WM. Imaging cerebral microbleeds using susceptibility weighted imaging: one step toward detecting vascular dementia. *Journal of Magnetic Resonance Imaging*. 2010;31(1):142-8.
18. Cordonnier C, Al-Shahi Salman R, Wardlaw J. Spontaneous brain microbleeds: systematic review, subgroup analyses and standards for study design and reporting. *Brain*. 2007;130(8):1988-2003.
19. de Rochefort L, Liu T, Kressler B, Liu J, Spincemaille P, Lebon V, et al. Quantitative susceptibility map reconstruction from MR phase data using bayesian regularization: validation and application to brain imaging. *Magnetic resonance in medicine*. 2010;63(1):194-206.
20. Wang Y, Liu T. Quantitative susceptibility mapping (QSM): decoding MRI data for a tissue magnetic biomarker. *Magnetic resonance in medicine*. 2015;73(1):82-101.
21. Liu T, Surapaneni K, Lou M, Cheng L, Spincemaille P, Wang Y. Cerebral microbleeds: burden assessment by using quantitative susceptibility mapping. *Radiology*. 2012;262(1):269-78.
22. Schweser F, Deistung A, Lehr BW, Reichenbach JR. Differentiation between diamagnetic and paramagnetic cerebral lesions based on magnetic susceptibility mapping. *Medical physics*. 2010;37(10):5165-78.
23. Haller S, Bartsch A, Nguyen D, Rodriguez C, Emch J, Gold G, et al. Cerebral microhemorrhage and iron deposition in mild cognitive impairment: susceptibility-weighted MR imaging assessment. *Radiology*. 2010;257(3):764-73.
24. Haacke EM, Mittal S, Wu Z, Neelavalli J, Cheng Y-C. Susceptibility-weighted imaging: technical aspects and clinical applications, part 1. *American Journal of Neuroradiology*. 2009;30(1):19-30.
25. Mittal S, Wu Z, Neelavalli J, Haacke EM. Susceptibility-weighted imaging: technical aspects and clinical applications, part 2. *American Journal of neuroradiology*. 2009;30(2):232-52.
26. Haacke EM, Xu Y, Cheng YCN, Reichenbach JR. Susceptibility weighted imaging (SWI). *Magnetic Resonance in Medicine: An Official Journal of the International Society for Magnetic Resonance in Medicine*. 2004;52(3):612-8.
27. Gregoire S, Werring D, Chaudhary U, Thornton J, Brown M, Yousry T, et al. Choice of echo time on GRE T2*-weighted MRI influences the classification of brain microbleeds. *Clinical radiology*. 2010;65(5):391-4.
28. Tustison NJ, Avants BB, Cook PA, Zheng Y, Egan A, Yushkevich PA, et al. N4ITK: improved N3 bias correction. *IEEE transactions on medical imaging*. 2010;29(6):1310.
29. Jenkinson M, Bannister P, Brady M, Smith S. Improved optimization for the robust and accurate linear registration and motion correction of brain images. *Neuroimage*. 2002;17(2):825-41.
30. Jenkinson M, Smith S. A global optimisation method for robust affine registration of brain images. *Medical image analysis*. 2001;5(2):143-56.
31. Greve DN, Fischl B. Accurate and robust brain image alignment using boundary-based registration. *Neuroimage*. 2009;48(1):63-72.
32. Doshi J, Erus G, Ou Y, Resnick SM, Gur RC, Gur RE, et al. MUSE: MULTI-atlas region Segmentation utilizing Ensembles of registration algorithms and parameters, and locally optimal atlas selection. *Neuroimage*. 2016;127:186-95.
33. Liu J, Liu T, de Rochefort L, Ledoux J, Khalidov I, Chen W, et al. Morphology enabled dipole inversion for quantitative susceptibility mapping using structural consistency between the magnitude image and the susceptibility map. *Neuroimage*. 2012;59(3):2560-8.
34. Bild DE, Bluemke DA, Burke GL, Detrano R, Diez Roux AV, Folsom AR, et al. Multi-ethnic study of atherosclerosis: objectives and design. *American journal of epidemiology*. 2002;156(9):871-81.
35. Olson JL, Bild DE, Kronmal RA, Burke GL. Legacy of MESA. *Global heart*. 2016;11(3):269-74.

36. Winston-Salem N, Irvine C. The multiethnic study of atherosclerosis. *Global heart*. 2016;11(3):267.
37. Heckbert SR, Austin TR, Jensen PN, Floyd JS, Psaty BM, Soliman EZ, et al. Yield and consistency of arrhythmia detection with patch electrocardiographic monitoring: The Multi-Ethnic Study of Atherosclerosis. *Journal of electrocardiology*. 2018;51(6):997-1002.
38. Çiçek Ö, Abdulkadir A, Lienkamp SS, Brox T, Ronneberger O, editors. 3D U-Net: learning dense volumetric segmentation from sparse annotation. *International conference on medical image computing and computer-assisted intervention*; 2016: Springer.
39. Ronneberger O, Fischer P, Brox T, editors. U-net: Convolutional networks for biomedical image segmentation. *International Conference on Medical image computing and computer-assisted intervention*; 2015: Springer.
40. Cohen CR, Duchesneau P, Weinstein M. Calcification of the basal ganglia as visualized by computed tomography. *Radiology*. 1980;134(1):97-9.
41. Modic M, Weinstein M, Rothner A, Erenberg G, Duchesneau P, Kaufman B. Calcification of the choroid plexus visualized by computed tomography. *Radiology*. 1980;135(2):369-72.
42. Kuijf HJ, Biesbroek JM, de Bresser J, Heinen R, Andermatt S, Bento M, et al. Standardized assessment of automatic segmentation of white matter hyperintensities; results of the wmh segmentation challenge. *IEEE transactions on medical imaging*. 2019.
43. Mendrik AM, Vincken KL, Kuijf HJ, Breeuwer M, Bouvy WH, De Bresser J, et al. MRBrainS challenge: online evaluation framework for brain image segmentation in 3T MRI scans. *Computational intelligence and neuroscience*. 2015;2015:1.
44. Roy S, Jog A, Magrath E, Butman JA, Pham DL, editors. Cerebral microbleed segmentation from susceptibility weighted images. *Medical Imaging 2015: Image Processing*; 2015: International Society for Optics and Photonics.
45. Kuijf HJ, de Bresser J, Geerlings MI, Conijn MM, Viergever MA, Biessels GJ, et al. Efficient detection of cerebral microbleeds on 7.0 T MR images using the radial symmetry transform. *NeuroImage*. 2012;59(3):2266-73.
46. Bian W, Hess CP, Chang SM, Nelson SJ, Lupo JM. Computer-aided detection of radiation-induced cerebral microbleeds on susceptibility-weighted MR images. *NeuroImage: clinical*. 2013;2:282-90.
47. Dou Q, Chen H, Yu L, Shi L, Wang D, Mok VC, et al., editors. Automatic cerebral microbleeds detection from MR images via independent subspace analysis based hierarchical features. 2015 37th annual international conference of the IEEE engineering in medicine and biology society (EMBC); 2015: IEEE.
48. Seghier ML, Kolanko MA, Leff AP, Jäger HR, Gregoire SM, Werring DJ. Microbleed detection using automated segmentation (MIDAS): a new method applicable to standard clinical MR images. *PloS one*. 2011;6(3):e17547.
49. Ashburner J, Friston KJ. Unified segmentation. *Neuroimage*. 2005;26(3):839-51.
50. Chen Y, Villanueva-Meyer JE, Morrison MA, Lupo JM. Toward Automatic Detection of Radiation-Induced Cerebral Microbleeds Using a 3D Deep Residual Network. *Journal of digital imaging*. 2018:1-7.
51. Liu S, Utriainen D, Chai C, Chen Y, Wang L, Sethi SK, et al. Cerebral microbleed detection using Susceptibility Weighted Imaging and deep learning. *NeuroImage*. 2019;198:271-82.
52. Dou Q, Chen H, Yu L, Zhao L, Qin J, Wang D, et al. Automatic detection of cerebral microbleeds from MR images via 3D convolutional neural networks. *IEEE transactions on medical imaging*. 2016;35(5):1182-95.
53. Habes M, Sotiras A, Erus G, Toledo JB, Janowitz D, Wolk DA, et al. White matter lesions: Spatial heterogeneity, links to risk factors, cognition, genetics, and atrophy. *Neurology*. 2018;91(10):e964-e75.

54. Nasrallah IM, Pajewski NM, Auchus AP, Chelune G, Cheung AK, Cleveland ML, et al. Association of intensive vs standard blood pressure control with cerebral white matter lesions. *Jama*. 2019;322(6):524-34.
55. Stehling C, Wersching H, Kloska SP, Kirchhof P, Ring J, Nassenstein I, et al. Detection of asymptomatic cerebral microbleeds: a comparative study at 1.5 and 3.0 T. *Academic radiology*. 2008;15(7):895-900.
56. Barnes SR, Haacke EM, Ayaz M, Boikov AS, Kirsch W, Kido D. Semiautomated detection of cerebral microbleeds in magnetic resonance images. *Magnetic resonance imaging*. 2011;29(6):844-52.
57. Fazlollahi A, Meriaudeau F, Villemagne VL, Rowe CC, Yates P, Salvado O, et al., editors. Efficient machine learning framework for computer-aided detection of cerebral microbleeds using the radon transform. 2014 IEEE 11th international symposium on biomedical imaging (ISBI); 2014: IEEE.

Table 1: Scanner parameters

Image Type	Echo Time (TE) (ms)	Repetition Time (TR) (ms)	Pixel Bandwidth (Hz/pixel)	Flip Angle (FA)	Slice Thickness (mm)	Acquisition Matrix	in-plane voxel size (mm)
T1 MPRAGE	2.93	1900	170	9	1	256x256	1x1
T2	408	3200	750	120	1	256x256	1x1
SWI	7.5, 15, 22.5, and 30	35	200	15	1.5	256x192	1x1

Table 2: Summary demographics for the included MESA participants (n=24).

Participants	Age	Sex	Number of CMBs (Average Size)	Iron deposits (voxel count)
4 participants	74-89	3 females, 1 male	0 CMBs (0 voxels or 0 mm ³)	4 participants had 96 – 326 voxels
13 participants	66-94	6 females, 7 males	1 or 2 CMBs (7.24 voxels or 10.85 mm ³)	11 participants had 9 – 283 voxels, 2 participants had 0 voxel)
6 participants	65-89	2 females, 4 males	3 to 8 CMBs (7.1 voxels or 10.21 mm ³)	4 participants had 2 – 146 voxels, 2 participants had 0 voxels
1 participant	67	1 male	120 (3.175 voxels or 4.76 mm ³)	0 voxels

Table 3: Experimental results with single class and multiclass prediction. The performance measures reported here are average sensitivity, average precision, average magnitude accuracy and false positives per participant, along with their respective standard errors of the mean (SEM) and the lower and upper bounds of the 95% confidence intervals (CI).

Labels	Modalities Used	Avg Sensitivity \pm SEM [CI: lower, upper]	Avg Precision \pm SEM [CI: lower, upper]	Avg Magnitude Accuracy \pm SEM [CI: lower, upper]	False Positives per Participant
Single Class CMB Only	SWI (baseline)	0.85 \pm 0.06 [0.74, 0.97]	0.22 \pm 0.04 [0.14, 0.31]	0.91 \pm 0.06 [0.80, 1.03]	7.21
	SWI and QSM	0.88 \pm 0.06 [0.77, 0.99]	0.40* \pm 0.07 [0.27, 0.54]	1.09* \pm 0.04 [1.00, 1.17]	4.33
	SWI and T2	0.84 \pm 0.07 [0.70, 0.97]	0.29 \pm 0.06 [0.17, 0.42]	0.95 \pm 0.08 [0.80, 1.10]	6.33
	SWI, QSM and T2	0.87 \pm 0.06 [0.76, 0.98]	0.50* \pm 0.07 [0.35, 0.64]	1.08* \pm 0.07 [0.94, 1.22]	2.79
Single Class Iron Deposits Only	SWI (baseline)	0.81 \pm 0.06 [0.68, 0.94]	0.51 \pm 0.07 [0.37, 0.65]	1.06 \pm 0.08 [0.91, 1.21]	3.29
	SWI and QSM	0.77 \pm 0.06 [0.65, 0.89]	0.60 \pm 0.07 [0.46, 0.75]	1.09 \pm 0.05 [0.99, 1.20]	2.71
	SWI and T2	0.77 \pm 0.06 [0.64, 0.89]	0.56 \pm 0.07 [0.42, 0.70]	1.04 \pm 0.08 [0.88, 1.19]	2.29
	SWI, QSM and T2	0.81 \pm 0.05 [0.71, 0.92]	0.62 \pm 0.07 [0.47, 0.76]	1.11 \pm 0.05 [1.02, 1.21]	2.50
Multiclass CMB	SWI (baseline)	0.82 \pm 0.07 [0.68, 0.96]	0.36 \pm 0.06 [0.24, 0.49]	0.99 \pm 0.06 [0.87, 1.12]	3.29
	SWI and QSM	0.84 \pm 0.07 [0.70, 0.98]	0.59* \pm 0.08 [0.43, 0.75]	1.15* \pm 0.07 [1.00, 1.29]	1.83
	SWI and T2	0.76 \pm 0.08 [0.60, 0.91]	0.43 \pm 0.06 [0.31, 0.56]	1.00 \pm 0.07 [0.86, 1.13]	2.50
	SWI, QSM and T2	0.89 \pm 0.05 [0.79, 1.00]	0.49 \pm 0.06 [0.37, 0.61]	1.07* \pm 0.06 [0.95, 1.19]	2.08
Multiclass Iron Deposits	SWI (baseline)	0.76 \pm 0.06 [0.63, 0.88]	0.70 \pm 0.08 [0.55, 0.86]	1.13 \pm 0.07 [0.99, 1.28]	1.29
	SWI and QSM	0.75 \pm 0.07 [0.62, 0.88]	0.75 \pm 0.08 [0.60, 0.91]	1.20 \pm 0.05 [1.11, 1.30]	1.29
	SWI and T2	0.76 \pm 0.06 [0.64, 0.89]	0.60 \pm 0.08 [0.44, 0.75]	1.08 \pm 0.07 [0.93, 1.22]	1.79
	SWI, QSM and T2	0.81 \pm 0.05 [0.71, 0.92]	0.64 \pm 0.08 [0.49, 0.79]	1.17 \pm 0.05 [1.08, 1.27]	1.88

* – Performance measure is statistically significant compared to the baseline (i.e. model trained with only SWI)

CI – lower, upper bounds of 95% confidence interval

SEM – Standard error of the mean

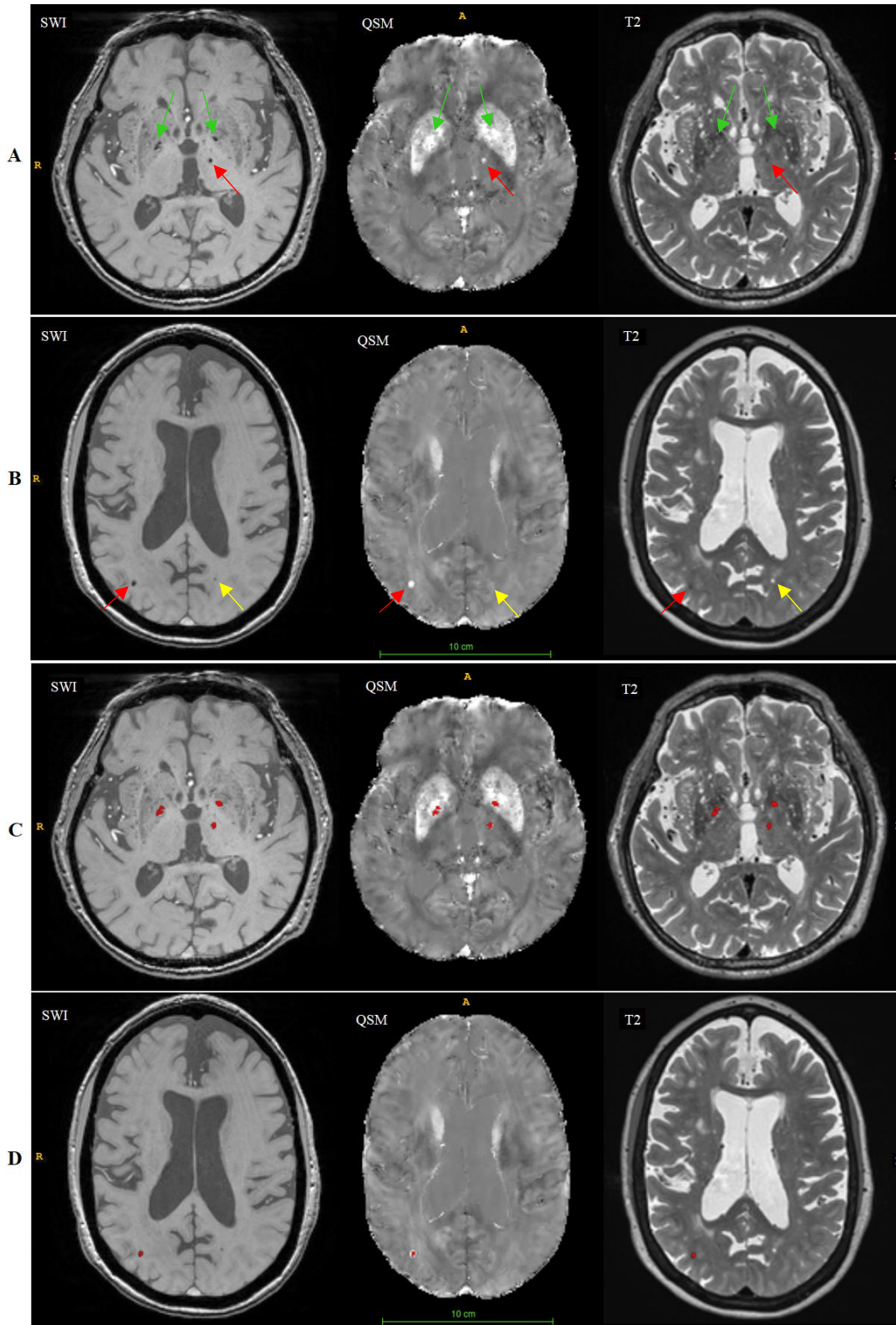


Figure 1: Panels A and B: Appearance of cerebral microbleeds (red arrow), iron deposits (green arrow) and enlarged perivascular spaces (yellow arrow) in susceptibility weighted imaging (left column), quantitative susceptibility mapping (middle column) and T2 (right column) for two participants. Panels C and D: Segmentations, in red color, of the CMBs and iron deposits generated by the deep learning model.

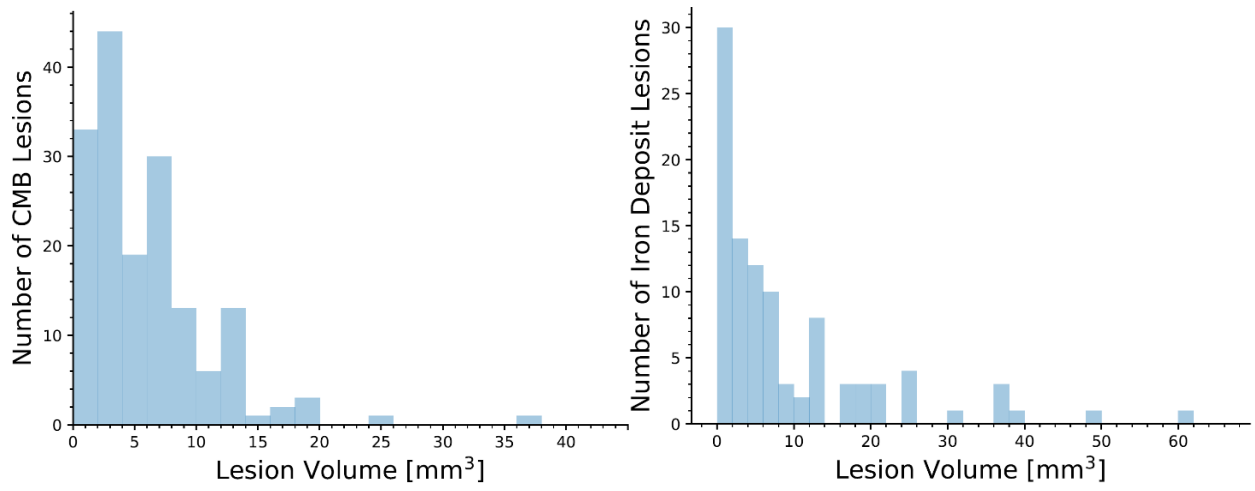


Figure 2: Histogram of the size of cerebral microbleeds (left panel) and iron deposits (right panel) lesions in mm³ pooled over all participants.

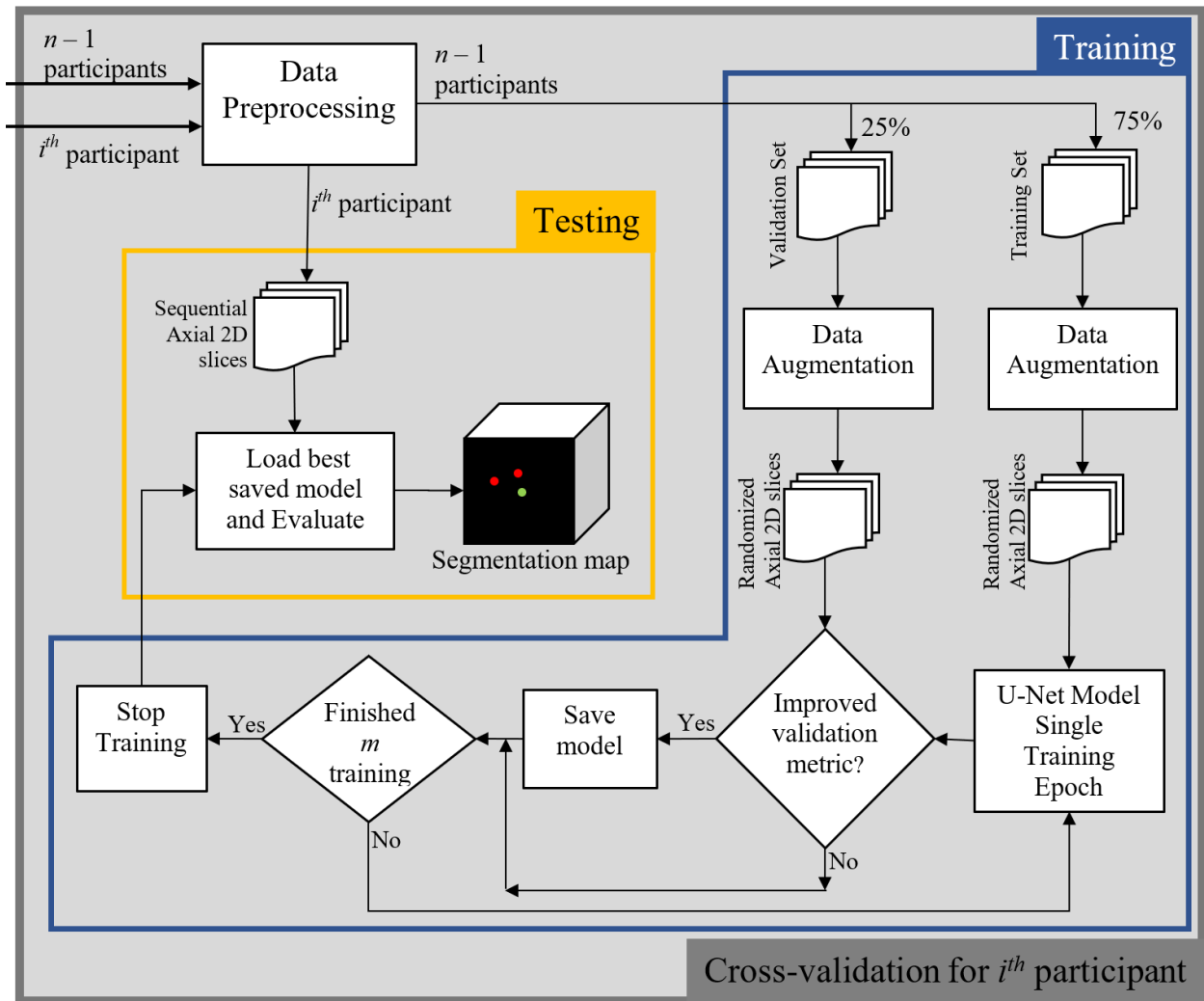


Figure 3: Overview of the split for one-fold of the cross-validation process that is repeated n times. In each fold, the model that was used to predict the test participant was trained on the remaining $n-1$ examples in order to avoid data leakage. Within the training stage, 25 percent of the $n-1$ participants were used as validation set. The model with highest validation accuracy was chosen to predict the left out participant example.

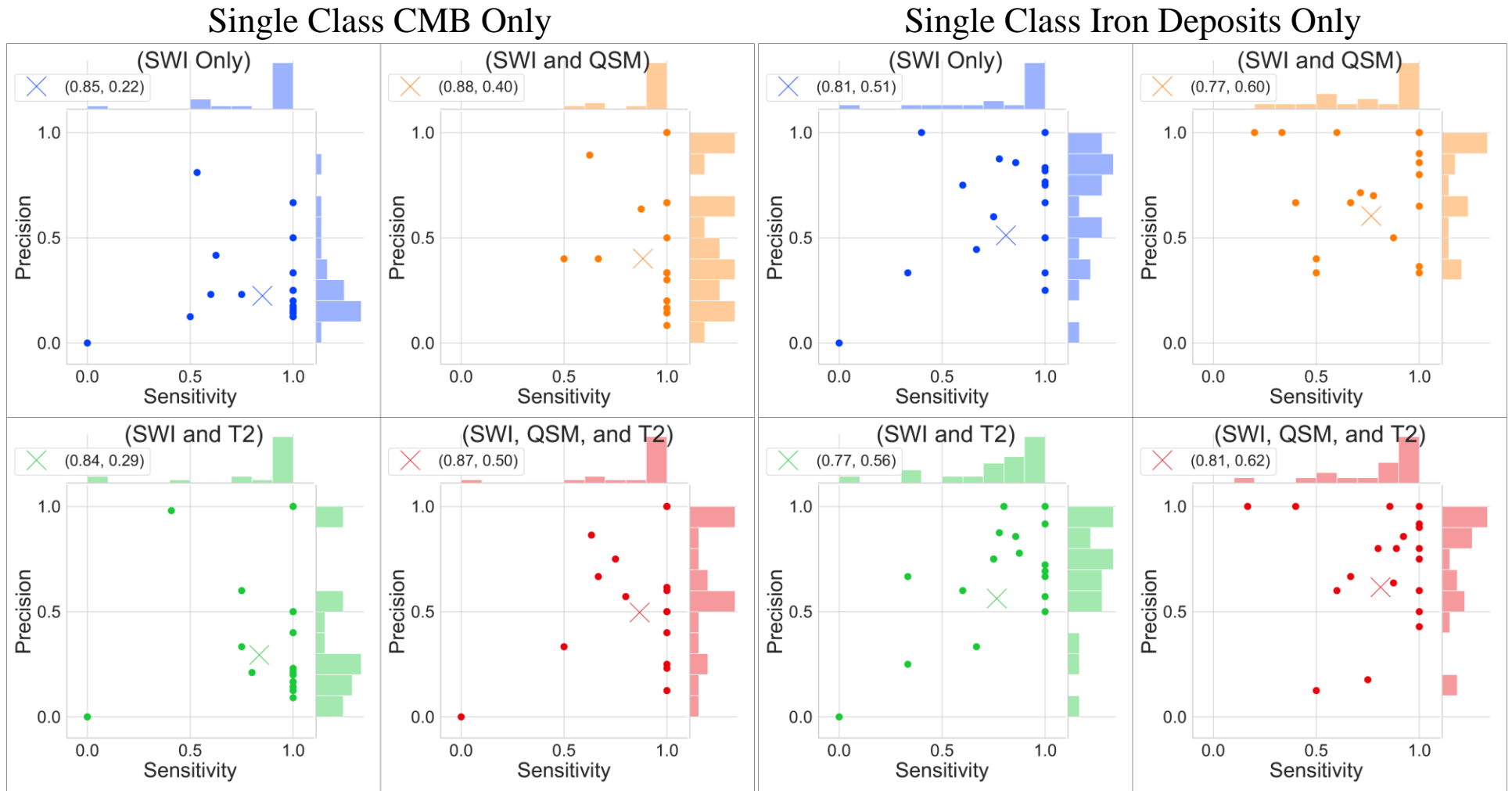


Figure 4: Joint scatterplots of the sensitivity vs precision of all single class experiments predicting CMBs and non-hemorrhage iron deposits. (Left) all CMB only experiments and (Right) all iron deposits only experiments. In each subplot, the round points indicate the individual participants' sensitivity and precision evaluated with leave-one-out cross-validation, and the X indicates the mean sensitivity and precision. The legend at the upper left corner of each subplot shows the coordinates of X. In each subplot, histograms of the sensitivity and precision are displayed along the upper and right axes.

Multiclass CMB

Multiclass Iron Deposits

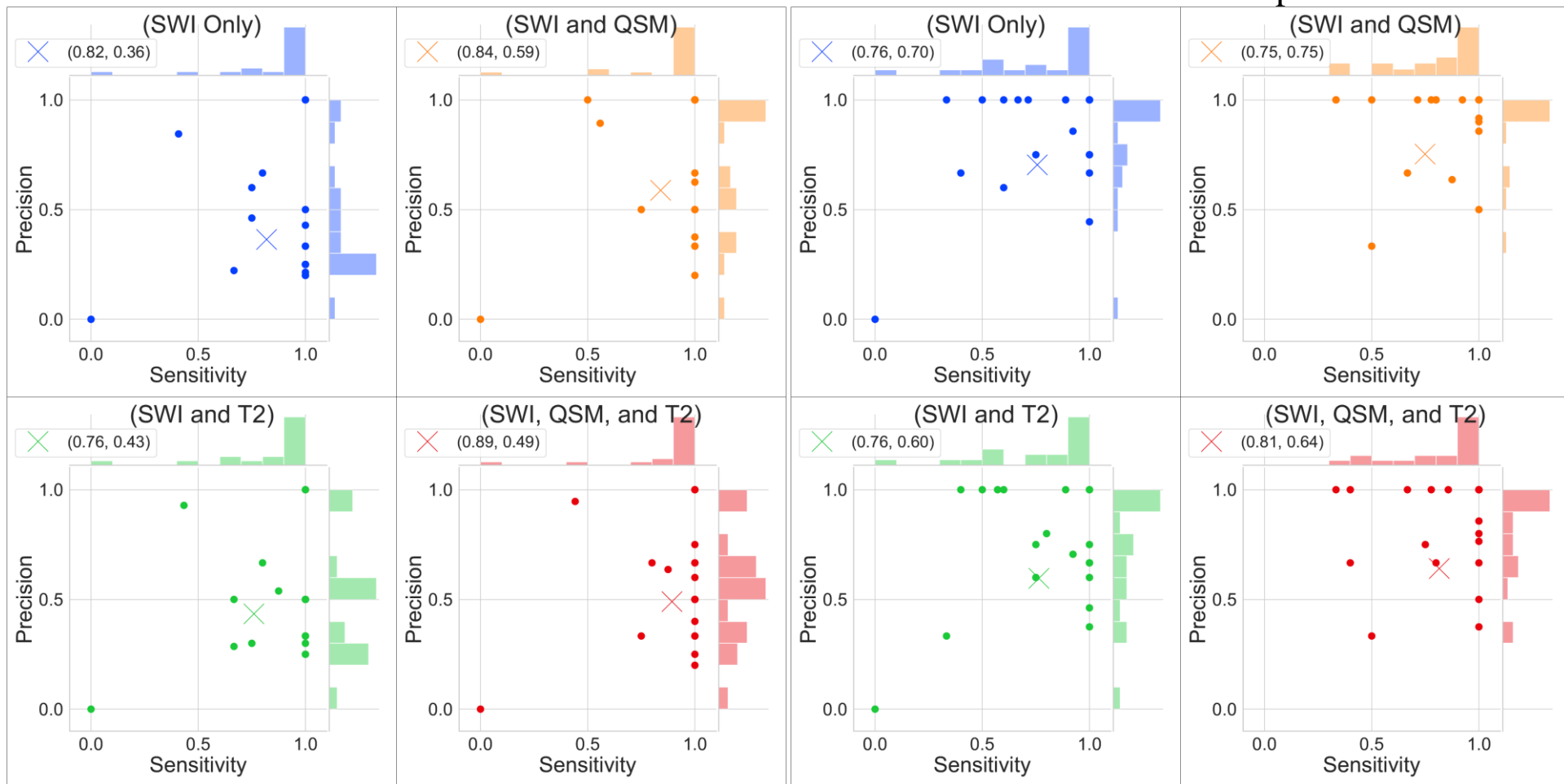
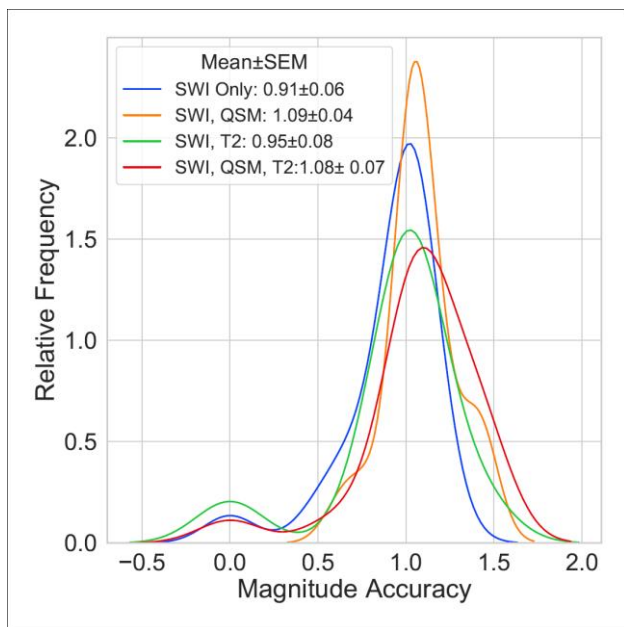
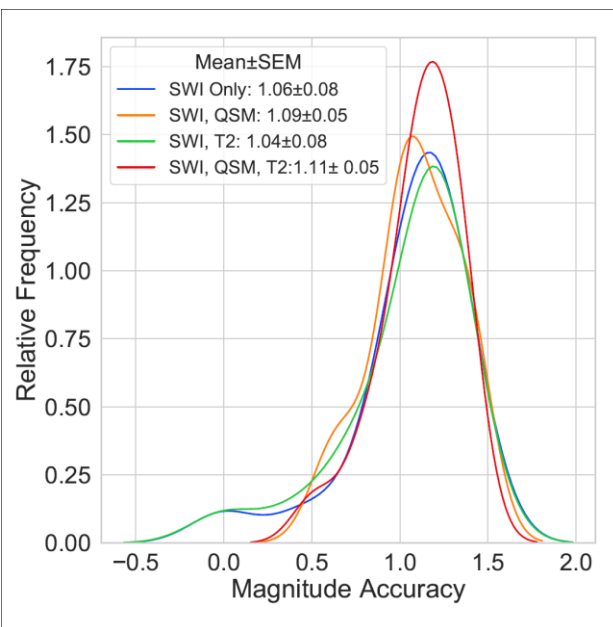


Figure 5: Joint scatterplots of the sensitivity vs precision of all multiclass experiments predicting CMBs and non-hemorrhage iron deposits. (Left) all evaluations for CMBs and (Right) all evaluations for iron deposits. In each subplot, the round points indicate the individual participants' sensitivity and precision evaluated with leave-one-out cross-validation, and the X indicates the mean sensitivity and precision. The legend at the upper left corner of each subplot shows the coordinates of X. In each subplot, histograms of the sensitivity and precision are displayed along the upper and right axes.

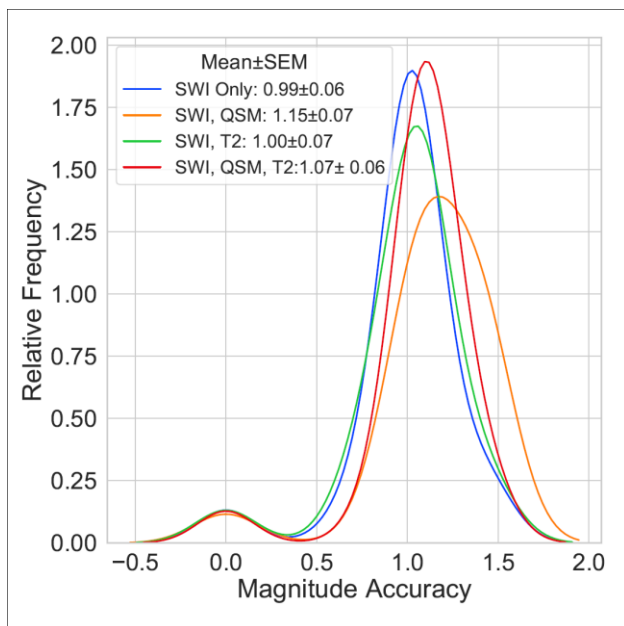
Single Class CMB Only



Single Class Iron Deposits Only



Multiclass CMB



Multiclass Iron Deposits

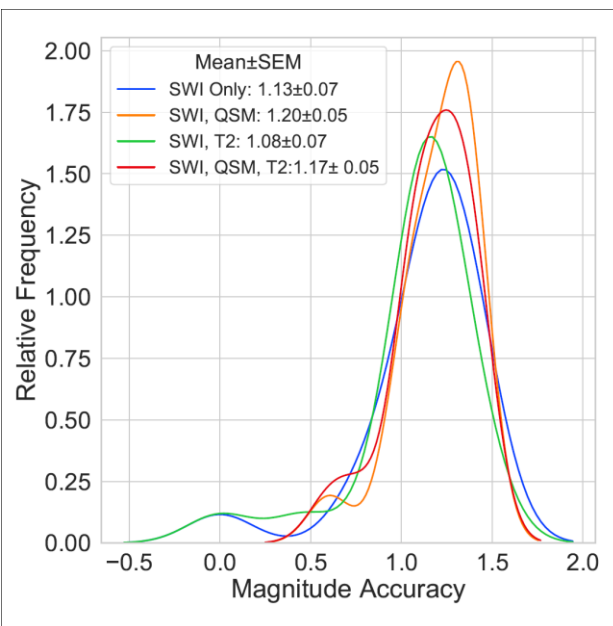


Figure 6: Histogram of the magnitude accuracy of all single class CMB only and non-hemorrhage iron deposits only experiments (top row) and multiclass CMB and non-hemorrhage iron deposit (bottom row) experiments. The legends in each subplot indicate the mean magnitude accuracy and standard error of the mean.

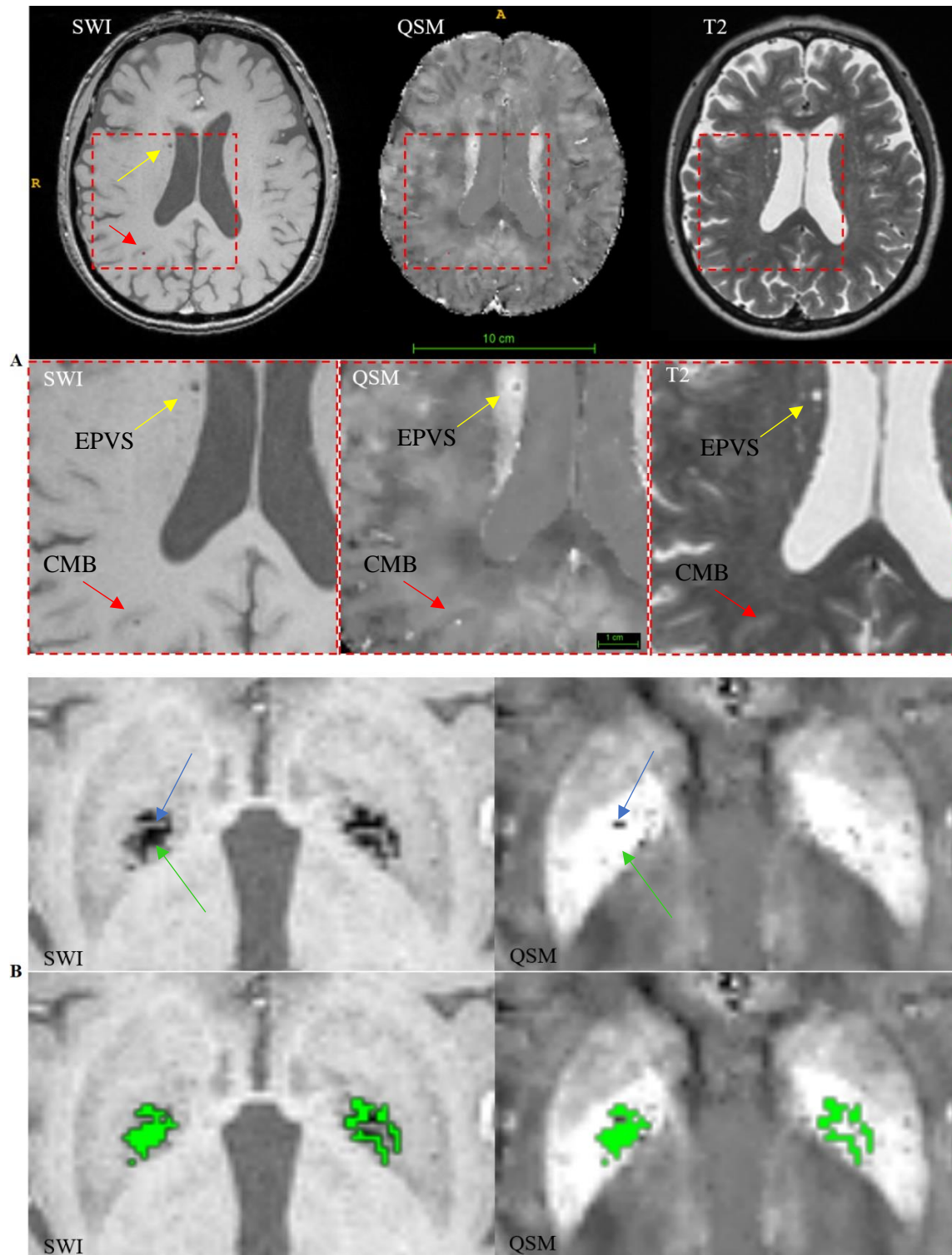


Figure 7: Panel A: (Top) An example of the correct segmentation of a microbleed (red segmentation of single pixel), and the correct rejection of an enlarged perivascular space. (Bottom) Magnified view of microbleed and mimic without segmentation masks. This segmentation is from the model trained with SWI, QSM and T2 images. Panel B: An example of being QSM used to distinguish iron deposits from calcifications. (Top row) The SWI and QSM of the basal ganglia. The blue arrow points to hypo-intense voxels which are likely calcifications and the green arrow points to basal ganglia iron deposits. (Bottom row) The segmentation (green labels) using the multi-class model trained with SWI, QSM and T2.

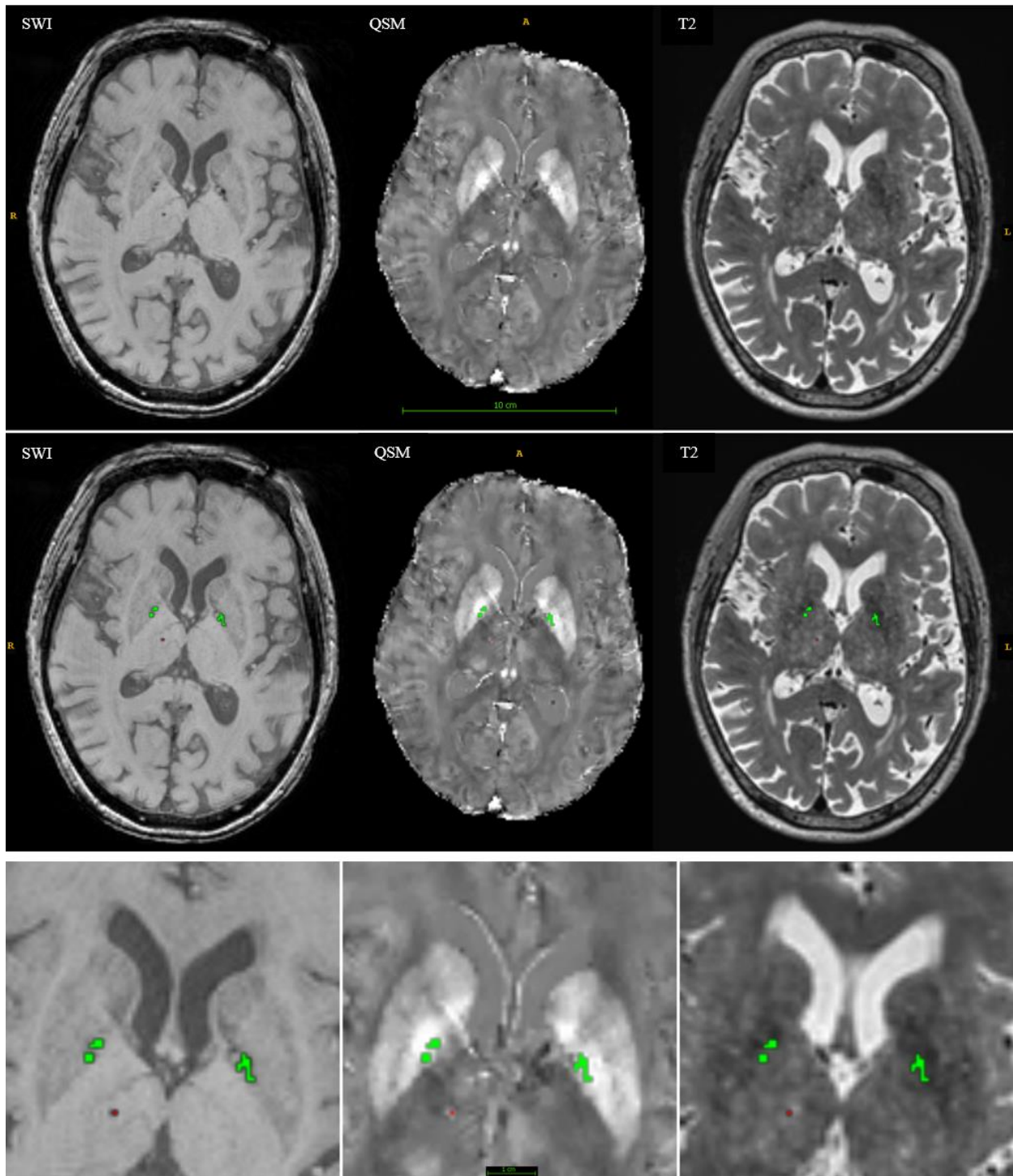


Figure 8: Segmentation result for multi-class model trained with SWI, QSM and T2. (Top row) Axial slices without segmentation masks, (middle row) with segmentation masks (bottom row) magnified view of the basal ganglia. CMBs are denoted as red segmentation and iron deposits are denoted with green segmentations.

Supplementary Materials 1 - Manual Annotation

S 1.1 Manual Annotation of CMBs and Non-hemorrhage Iron Deposits

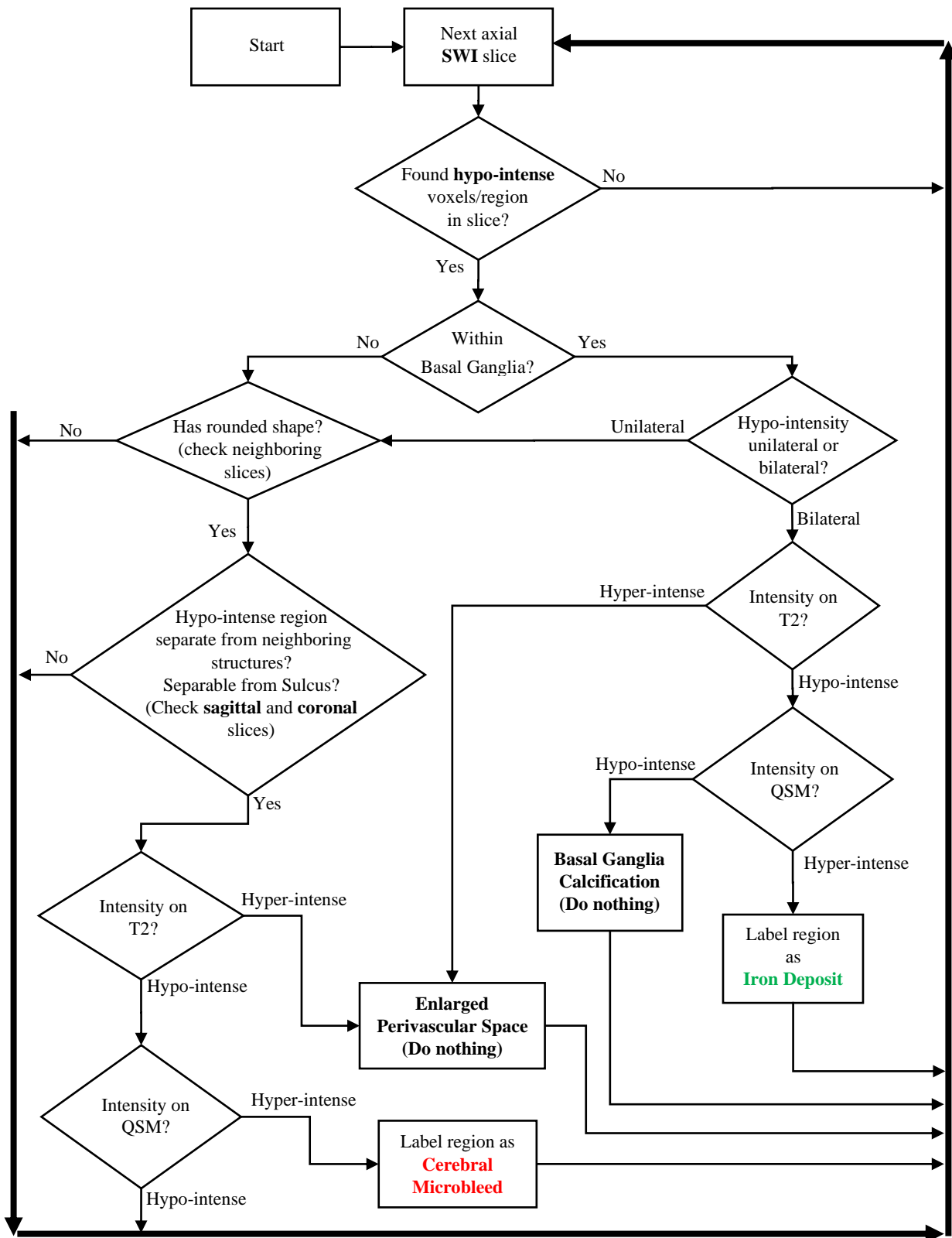
Current rating scales for CMBs such as MARS [1] and BOMBS [2] provide only coarse information about the spatial location and shape of CMBs. They were not designed to individually detect and annotate individual CMBs on the MR image itself, which limits their usefulness for training machine learning models. To address this, we implemented a custom protocol (shown in Figure S 1) to simultaneously annotate CMBs and non-hemorrhage iron deposits in the basal ganglia while ignoring EPVSs and calcifications. Our custom protocol was inspired by the systemic approach of the Brain Observer MicroBleed Scale (BOMBS) [2]. CMBs and non-hemorrhage iron deposits were annotated by experts (IMN and TR) with integer values 1 and 2, respectively. The manual annotation is based on the following observations:

1. CMBs and iron deposits are hypo-intense on SWI, hyper-intense on QSM and have some hypo-intensity on T2,
2. CMBs are rounded in shape and can appear anywhere in the brain,
3. Non-hemorrhage iron deposits do not have any specific shape but are generally larger than CMBs and are mainly located in the gray matter of the basal ganglia, particularly the globus pallidus
4. Similar to the characteristics of CMBs and iron deposits described in MARS, if a hypo-intensity on SWI occurs unilaterally, i.e. on one side of the basal ganglia then it is more likely to be a CMB, and if the hypo-intensity is bilateral, then it is assumed to be non-hemorrhage iron deposits.

The annotation protocol is as follows: For each axial SWI slice having a rounded hypo-intense region (candidate region) similar to CMBs:

1. Inspect the previous and next few slices to ensure that the rounded hypo-intense region is not a part of other structures such as blood vessels or sulcus. If it is a part of a blood vessel or similar elongated linear structure, then the rounded hypointense region will be prevalent in several adjacent axial slices (more than 5 slices). If the rounded hypointense region is part of the sulci, then the hypointense region will seem to join with the sulci in subsequent slices. It may be necessary to inspect the candidate region in sagittal and coronal slices to verify.
2. Once it has been confirmed that the rounded hypo-intense region is separate and not part of other structures, check the region's corresponding intensities on the T2 and QSM images.
 - a. If the corresponding region is hyper-intense on the T2 image, and shows no appreciable change in intensity on the QSM compared to surrounding voxels, then the region likely represents an enlarged perivascular space.

- b. If the corresponding region is hypo-intense or does not show any discernable changes in intensity on the T2 compared to surrounding voxels, and hyperintense on the QSM image, then the region likely represents a CMB.
3. If the region within the globus pallidus section of the basal ganglia is hypo-intense on the SWI, hyper-intense on the QSM, and show some hypo-intensity on the T2 image compared to surrounding voxels, then the region represents non-hemorrhage iron deposits. On the other hand, if the region is hypo-intense on the QSM, then the region likely represents calcium deposits.



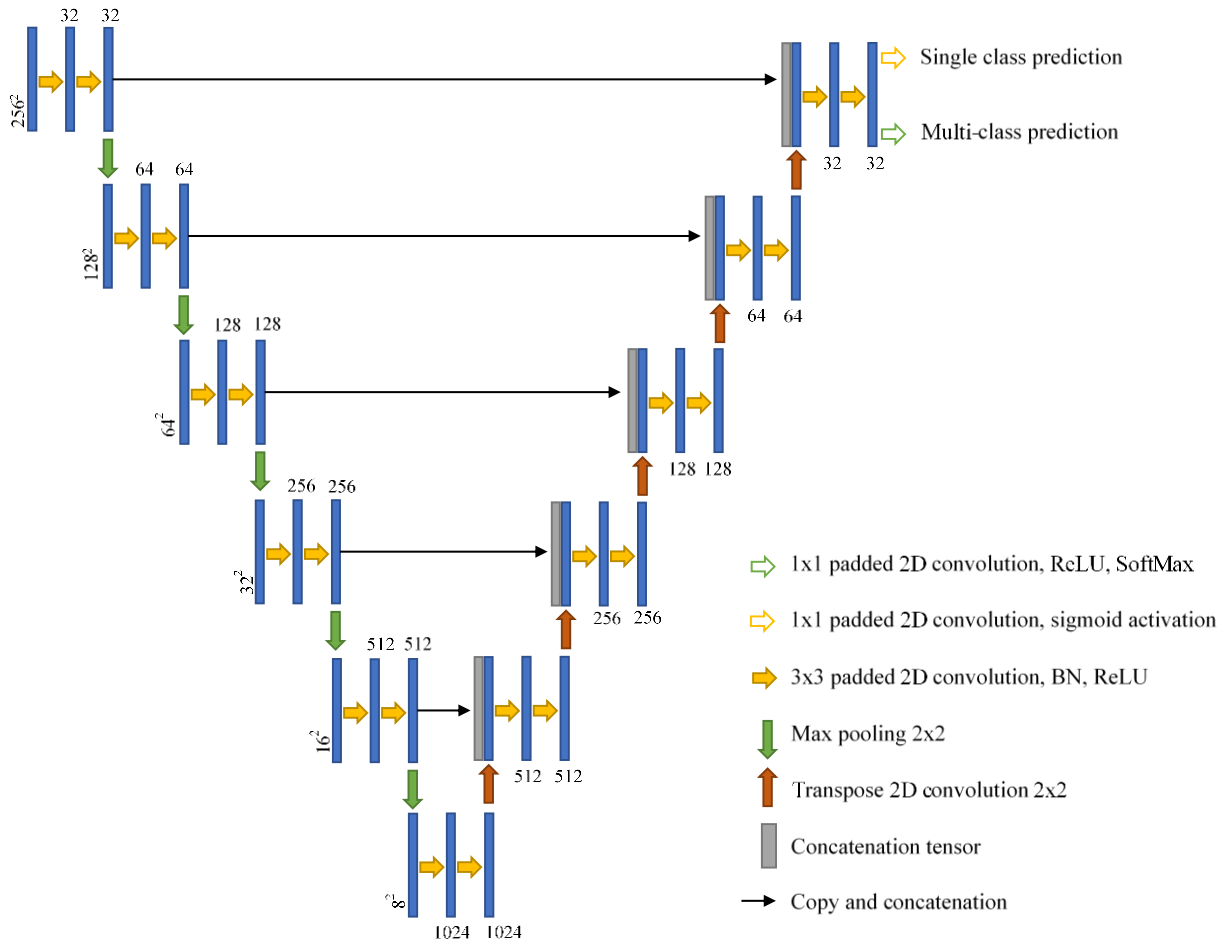
S 1: Flowchart for labeling cerebral microbleeds, iron deposits, basal ganglia calcifications and enlarged perivascular spaces.

Supplementary Materials 2 - 2D U-Net

S 2.1 2D U-Net with Padded Convolutions

Our lesion prediction models are based on the U-Net [3]. Both single and multi-class models consist of an analysis path (down-sampling operations) with five stages of convolution blocks and pooling, followed by a five synthesis path (up-sampling) with five stages of up-convolutions, plus a convolutional block. Each downsampling block consists of two layers of a 2D padded convolution layer having kernel size of 3x3 and stride of 1x1, followed by Batch Normalization and ReLU activation. The downsampling block ends with a 2x2 max pooling layer which reduces the resolution feature map by half in every spatial direction. The central block consists of two instances of padded 2D convolution with kernel size 3x3 and stride 1x1, followed by Batch Normalization and ReLU activation. Each upsampling block passes its input data through a 2D transpose convolution with kernel size of 2x2 and stride 2x2 in order to double the size of the feature map. This doubled feature map is then concatenated with the feature map (same size) of the corresponding analysis stage (i.e. the feature map before max pooling layer), followed by two instances of a padded 2D convolution layer having kernel size 3x3 and stride 1x1, followed by Batch Normalization and ReLU activation. Due to the use of padded convolutions throughout the model, the input and output image sizes are the same (256x256). The smallest downsampled image size is 8x8 in the central convolution block.

In the case of the single class prediction model, the output of the final upsampling stage passes through a 2D convolution layer with kernel size 1x1, stride 1x1 and Sigmoid activation function. For the multi-class prediction model, the output of the final upsampling block is passed through a 2D convolution layer with kernel size 1x1, stride 1x1 and ReLU activation function, and then through a SoftMax layer to generate class probabilities. The model architecture is depicted in Supplementary Figure S 2. We employed, random translations, random rotation, and flipping along the left-right axis during training. The network was trained with the cross-entropy loss.



S 2: U-Net architecture using padded convolutions for both single class and multi-class predictions.

Supplementary Materials 3: Additional Details on Experimental Pipeline

S 3.1 Image Preprocessing

Each input image was normalized to have zero mean and unit variance. For QSM images, an additional prior step truncated the overall intensity such that the intensity was within the range $[-k * \sigma_{QSM} \leq V_{QSM} \leq k * \sigma_{QSM}]$, where $k = 5$ and σ_{QSM} is the standard deviation for the QSM image. This step is necessary because QSM images contain high intensity noise (especially around the boundary of the brain and the region proximate to the sinus cavity) which may de-emphasize the intensity of the rest of the brain.

S 3.2 Data Augmentation

To improve the robustness of the deep learning network and include more training data we enriched the training and validation datasets with augmentation. Axial slices containing CMBs and iron deposits are, for the most part, few compared to the remaining slices in a given brain volume. This type of class imbalance may bias the training process. To address this, data augmentation was performed on slices selectively instead of all slices, inspired from the concept of random over-sampling (ROS) and random under-sampling (RUS) [4]. First, all slices containing the labels of interest (i.e. CMBs and/or iron deposits) are augmented. Then a number of the remaining slices are randomly selected and augmented in the same manner until the total number of slices containing the labels of interest and the total number of slices that do not contain any labels of interest is similar.

Data augmentation consisted of geometric transforms such as translations, rotations and image mirroring. In each experiment, the axial SWI slice (along with the corresponding axial QSM and T2 slices) and corresponding axial reference annotation slice was augmented. For translations, a set of two random integers tx and ty (representing the amount of shift per axis) were generated within the range $[-45, 45]$ and used to translate the image slice(s) and corresponding slice of the reference annotation. This range was chosen empirically so that most of the brain would be visible in the translated image. For practical purposes, for single class segmentations a total of 6 random integers were generated for each set of translations per axis, and 10 random integers per axis were generated for multi-class segmentations.

For rotations, a set of random integers d (representing the rotation in degree) were generated within the range $[1, 60]$, and the image slice(s) and the slices with reference annotations were rotated using both $+d$ and $-d$. The regions of the crops that were located outside the image matrix were padded with edge values. For single class segmentation, a total of 6 random integers were used for practical purposes and a total of 16 random integers were used for multi-class experiments.

S 3.3 Experiment with Combined CMB U Iron Deposit Labels

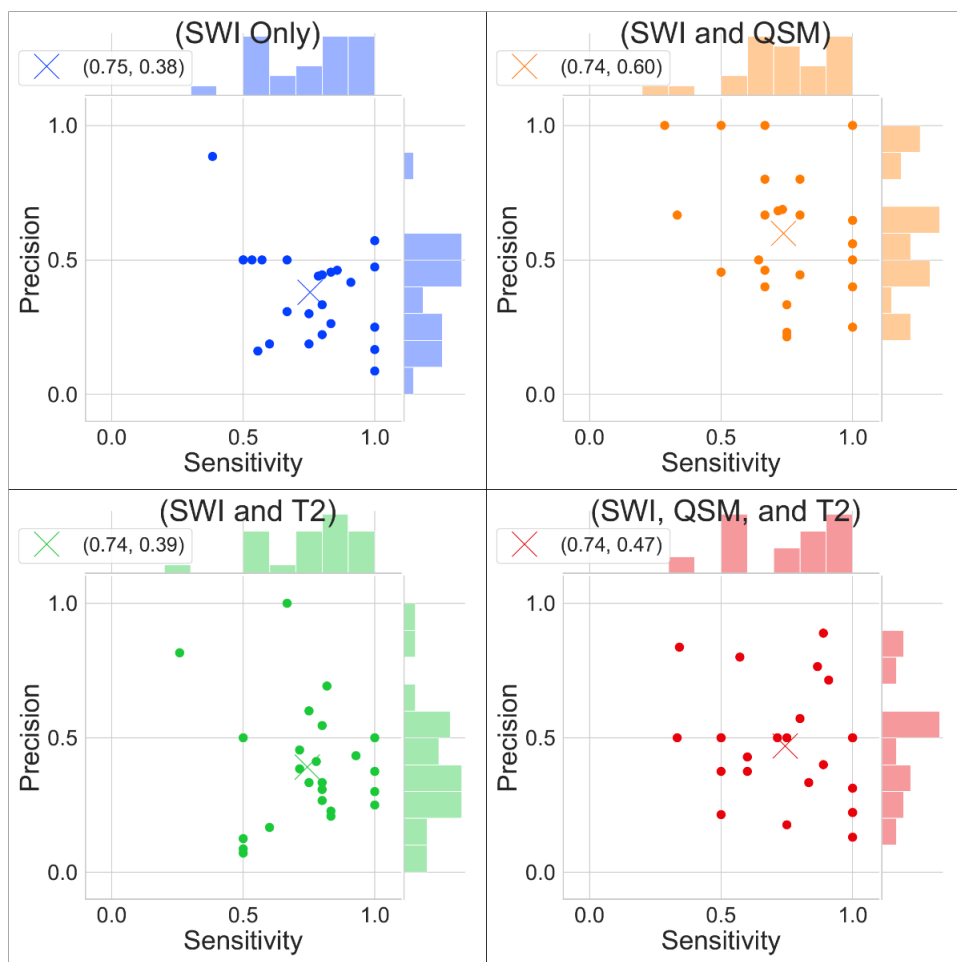
As discussed previously, both CMBs and non-hemorrhage iron deposits have similar MR signal characteristics in SWI, QSM and T2. The only readily observable difference between CMBs and iron deposits is their shape: CMBs have a distinctive spherical/ellipsoidal shape whereas non-hemorrhage iron deposits do not. An experiment was performed where both CMBs and iron deposits were set to the same label value, i.e. CMBs U iron deposits.

In the case of combined CMB and non-hemorrhage iron deposit labels, the best performing model was the one trained with SWI and QSM with average sensitivity, precision and magnitude accuracy of 0.74, 0.60 and 0.98, respectively with 6.04 FPs per participant. The model trained with SWI, QSM and T2 had the next best performance in terms of magnitude accuracy (0.91), with average sensitivity and precision of 0.74 and 0.47, respectively with 7.25 FPs per participant. When compared against the baseline model, both precision and magnitude accuracy for the model trained with SWI and QSM were better ($p = 0.003$ and $p = 0.021$, respectively). The results of all the experiments using combined CMB and non-hemorrhage iron deposit labels is detailed in Table S3.1. Figure S3 show the joint scatterplots of the sensitivity vs precision, and Figure S4 show the histogram of the magnitude accuracy, for all the experiments where the combined CMB and non-hemorrhage iron deposit labels were used.

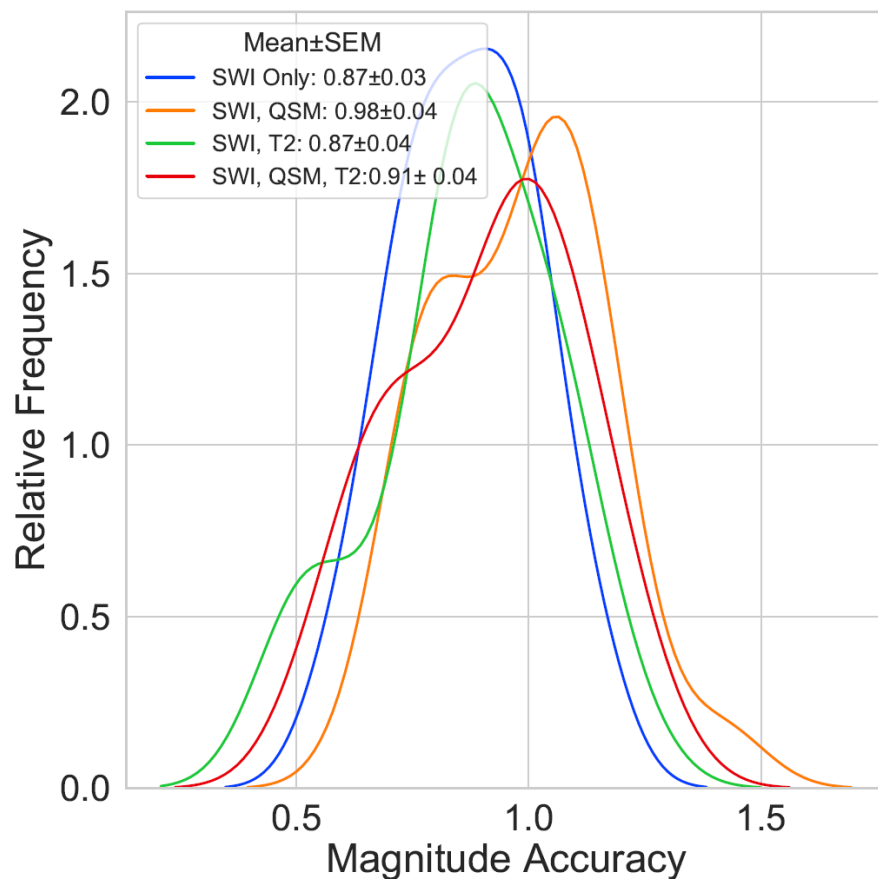
Table S3.1: Experimental results with single class prediction using combined CMB and iron deposit labels. The performance measures reported here are average sensitivity, average precision, average magnitude accuracy and false positives per participant, along with their respective standard errors of the mean (SEM) and the lower and upper bounds of the 95% confidence intervals (CI).

Labels	Modalities Used	Avg Sensitivity \pm SEM [CI: lower, upper]	Avg Precision \pm SEM [CI: lower, upper]	Avg Magnitude Accuracy \pm SEM [CI: lower, upper]	False Positives per Participant
Single Class CMB U Iron Deposits	SWI (baseline)	0.75 \pm 0.04 [0.68, 0.83]	0.38 \pm 0.04 [0.31, 0.45]	0.87 \pm 0.03 [0.81, 0.93]	10.00
	SWI and QSM	0.74 \pm 0.04 [0.66, 0.82]	0.60* \pm 0.05 [0.50, 0.70]	0.98* \pm 0.04 [0.91, 1.05]	6.04
	SWI and T2	0.74 \pm 0.04 [0.67, 0.82]	0.39 \pm 0.05 [0.30, 0.48]	0.87 \pm 0.04 [0.79, 0.94]	10.54
	SWI, QSM and T2	0.74 \pm 0.04 [0.66, 0.83]	0.47 \pm 0.04 [0.39, 0.55]	0.91 \pm 0.04 [0.83, 0.99]	7.25

Joint Scatterplot for Iron Deposits U CMB



Histogram for Iron Deposits U CMB



S 3: (Left) Joint scatterplots of the sensitivity vs precision for experiments where the combined iron deposit and CMB labels were used. In each subplot, the round points indicate the individual participants' sensitivity and precision evaluated with leave-one-out cross-validation, and the X indicates the mean sensitivity and precision. The legend at the upper left corner of each subplot shows the coordinates of X. In each subplot, histograms of the sensitivity and precision are displayed along the upper and right axes. (Right) Histogram of the magnitude accuracy of all single class experiments where the combined iron deposit and CMB labels were evaluated. The legends in each subplot indicate the mean magnitude accuracy and standard error of the mean.

Supplementary Materials 4: Additional Experimental Results

S 4.1 Outlier Detection

In our training and testing dataset, there is a single participant with more than 100 CMBs. As shown in Figure S3, a beta distribution fitted to the number of CMBs in this dataset indicates that the 99th percentile of the distribution is approximately 16 CMBs. The participant with more than 100 CMBs is clearly an outlier by this definition.

It should be noted that under different circumstances this participant may not be considered an outlier in terms of the number of CMBs. Large numbers of CMBs have been observed in patients with vascular pathologies such as cerebral amyloid angiopathy (CAA) [5] or hypertension [6].

S 4.2 Experiments Results

In this series of experiments, model training and testing using leave-one-out cross-validation is conducted with the participant with more than 100 CMBs being treated as an outlier and excluded from the dataset. All other training and testing parameters were kept the same as the experiments in the main paper. The non-parametric two-tailed Wilcoxon rank sum test to check for statistical significance statistical significance in the sensitivity, precision and magnitude accuracy for each type of experiment. Comparisons were made against the model trained with only SWI. All statistical testing was performed using MATLAB R2017b.

S 4.2.1 Single Class Model

The results for experiments based on the single class models are reported in Table S4.1. For detecting only CMBs the best model in terms of magnitude accuracy (1.09) was the one trained with SWI, QSM and T2, having an average sensitivity and precision of 0.85 and 0.45 respectively and false positives (FPs) per participant of 3.04. A comparison against the baseline model (the model trained with only SWI) revealed that the magnitude accuracy for this model was statistically significant ($p = 0.046$).

For the task of detecting iron deposits only, the best model was the one trained with SWI and QSM having an average sensitivity and precision of 0.80 and 0.64, respectively, with a magnitude accuracy of 1.12 and 1.61 FPs per participant. Statistical testing against the baseline model did not reveal any statistically significant differences for the sensitivity, precision or magnitude accuracy.

Figure S5 shows the joint scatterplots of the sensitivity and precision for all the single class experiments involving CMBs only and non-hemorrhage iron deposits only. Figure S8 (top row) shows the histograms of the magnitude accuracy of the single class experiments involving CMBs only and non-hemorrhage iron deposits only.

In the case of combined CMB and iron deposit labels, the best performing model was the one trained with SWI, QSM and T2 with average sensitivity, precision and magnitude accuracy of 0.70, 0.51 and 0.895,

respectively and 6.30 FPs per participant. Statistical testing against the baseline model did not reveal any statistically significant differences for the sensitivity, precision or magnitude accuracy. Figure S6 (left) shows the joint scatterplot of the sensitivity vs precision and Figure S6 (right) shows the histogram of the magnitude accuracy of all experiments where the combined CMB and iron deposit labels were evaluated.

S 4.2.2 Multi-class Model

In this analysis, CMBs and iron deposits were treated as individual types of lesions and predicted/evaluated simultaneously. The corresponding results are reported in Table S4.2. In the case of CMB detection, the model trained with SWI and T2 had the best performance in terms of average magnitude accuracy of 1.18, with average sensitivity and precision of 0.86 and 0.62, respectively with 1.22 FPs per participant. A comparison against the baseline model (the model trained with only SWI) revealed that the magnitude accuracy for this model was statistically significant ($p = 0.016$).

For detecting iron deposits with the multi-class models, the best performing models in terms of average magnitude accuracy (1.17) were the ones trained with SWI and T2, and SWI and QSM. Both models achieved similar precisions of 0.66, however the model trained with SWI and T2 had the higher average sensitivity of 0.87. However, statistical testing against the baseline model did not reveal any statistically significant differences for the sensitivity, precision or magnitude accuracy. Figure S7 shows the joint scatterplots of the sensitivity and precision for the multiclass experiments. Figure S8 (bottom row) shows the histograms of the magnitude accuracy of the multiclass experiments.

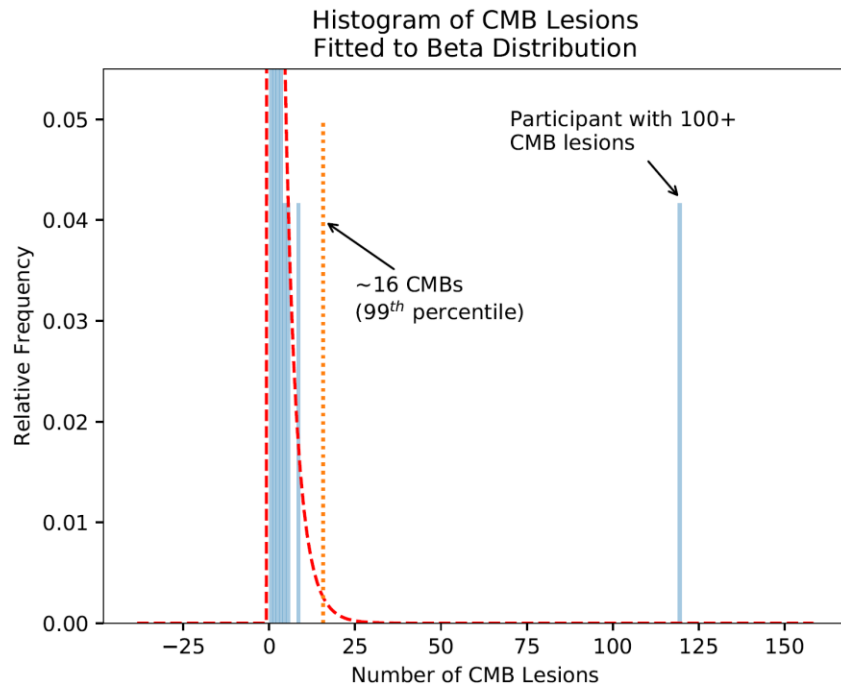
Table S4.1: Table 4: Experimental results with single class and multiclass prediction models without outlier. The performance measures reported here are average sensitivity, average precision, average magnitude accuracy and false positives per participant, along with their respective standard errors of the mean (SEM) and the lower and upper bounds of the 95% confidence intervals (CI).

Labels	Modalities Used	Avg Sensitivity \pm SEM [CI: lower, upper]	Avg Precision \pm SEM [CI: lower, upper]	Avg Magnitude Accuracy \pm SEM [CI: lower, upper]	False Positives per Participant
Single Class CMB Only	SWI (baseline)	0.76 \pm 0.09 [0.59, 0.93]	0.30 \pm 0.06 [0.18, 0.43]	0.86 \pm 0.10 [0.67, 1.05]	4.57
	SWI and QSM	0.81 \pm 0.08 [0.65, 0.96]	0.43 \pm 0.07 [0.29, 0.57]	0.97 \pm 0.09 [0.79, 1.14]	2.00
	SWI and T2	0.86 \pm 0.07 [0.72, 1.00]	0.35 \pm 0.07 [0.22, 0.49]	0.98 \pm 0.09 [0.81, 1.15]	4.26
	SWI, QSM and T2	0.85 \pm 0.07 [0.71, 0.99]	0.45 \pm 0.08 [0.29, 0.60]	1.09* \pm 0.07 [0.94, 1.23]	3.04
Single Class CMB U Iron Deposits	SWI (baseline)	0.70 \pm 0.05 [0.60, 0.81]	0.49 \pm 0.06 [0.39, 0.60]	0.89 \pm 0.06 [0.77, 1.01]	6.35
	SWI and QSM	0.73 \pm 0.04 [0.64, 0.81]	0.47 \pm 0.03 [0.41, 0.54]	0.89 \pm 0.04 [0.82, 0.96]	6.17
	SWI and T2	0.68 \pm 0.04 [0.59, 0.76]	0.46 \pm 0.05 [0.37, 0.55]	0.83 \pm 0.05 [0.72, 0.94]	6.09
	SWI, QSM and T2	0.70 \pm 0.03 [0.63, 0.76]	0.51 \pm 0.05 [0.40, 0.61]	0.89 \pm 0.04 [0.82, 0.97]	6.30
Single Class Iron Deposits Only	SWI (baseline)	0.80 \pm 0.06 [0.68, 0.93]	0.54 \pm 0.07 [0.40, 0.68]	1.05 \pm 0.08 [0.90, 1.20]	2.87
	SWI and QSM	0.80 \pm 0.06 [0.68, 0.92]	0.64 \pm 0.07 [0.50, 0.77]	1.12 \pm 0.05 [1.01, 1.22]	1.61
	SWI and T2	0.74 \pm 0.07 [0.60, 0.89]	0.51 \pm 0.07 [0.37, 0.65]	0.99 \pm 0.08 [0.83, 1.16]	3.13
	SWI, QSM and T2	0.76 \pm 0.07 [0.62, 0.90]	0.56 \pm 0.08 [0.41, 0.71]	1.06 \pm 0.07 [0.92, 1.20]	2.78
Multiclass CMB	SWI (baseline)	0.72 \pm 0.08 [0.56, 0.88]	0.46 \pm 0.06 [0.34, 0.59]	1.03 \pm 0.04 [0.96, 1.11]	1.61
	SWI and QSM	0.85 \pm 0.07 [0.71, 0.98]	0.55 \pm 0.08 [0.39, 0.71]	1.11 \pm 0.08 [0.96, 1.26]	1.52
	SWI and T2	0.86 \pm 0.06 [0.74, 0.98]	0.62 \pm 0.07 [0.48, 0.77]	1.18* \pm 0.04 [1.10, 1.27]	1.22
	SWI, QSM and T2	0.89 \pm 0.06 [0.78, 1.00]	0.48 \pm 0.07 [0.34, 0.61]	1.07 \pm 0.07 [0.93, 1.21]	2.17
Multiclass Iron Deposits	SWI (baseline)	0.84 \pm 0.05 [0.74, 0.93]	0.65 \pm 0.07 [0.51, 0.79]	1.16 \pm 0.05 [1.07, 1.26]	1.39
	SWI and QSM	0.80 \pm 0.07 [0.67, 0.94]	0.66 \pm 0.07 [0.52, 0.80]	1.17 \pm 0.05 [1.07, 1.27]	2.00
	SWI and T2	0.87 \pm 0.04 [0.78, 0.95]	0.66 \pm 0.07 [0.52, 0.79]	1.17 \pm 0.05 [1.08, 1.26]	1.57
	SWI, QSM and T2	0.77 \pm 0.08 [0.62, 0.93]	0.56 \pm 0.07 [0.42, 0.71]	1.06 \pm 0.09 [0.89, 1.23]	2.22

* – Performance measure is statistically significant compared to the baseline (i.e. model trained with only SWI)

CI – lower, upper bounds of 95% confidence interval

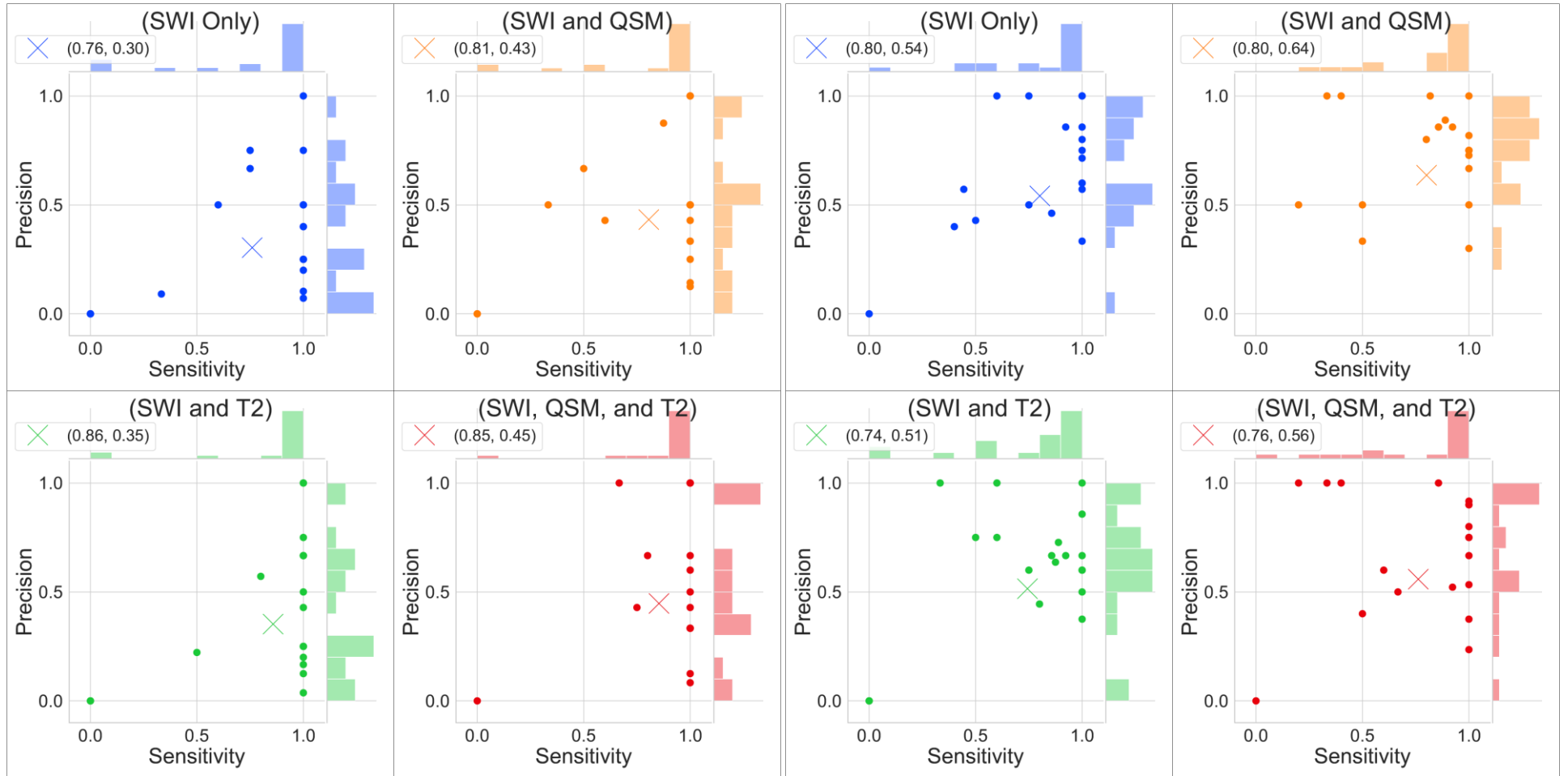
SEM – Standard error of the mean



S 4: A histogram of the number of CMB lesions. The blue columns represent the number of lesions. A beta distribution is fitted to this histogram (red dashed curve). The 99th percentile of this distribution (orange dotted line) is approximately 16 CMBs. The blue bar towards the right of the figure is the participant with more than 100 CMBs.

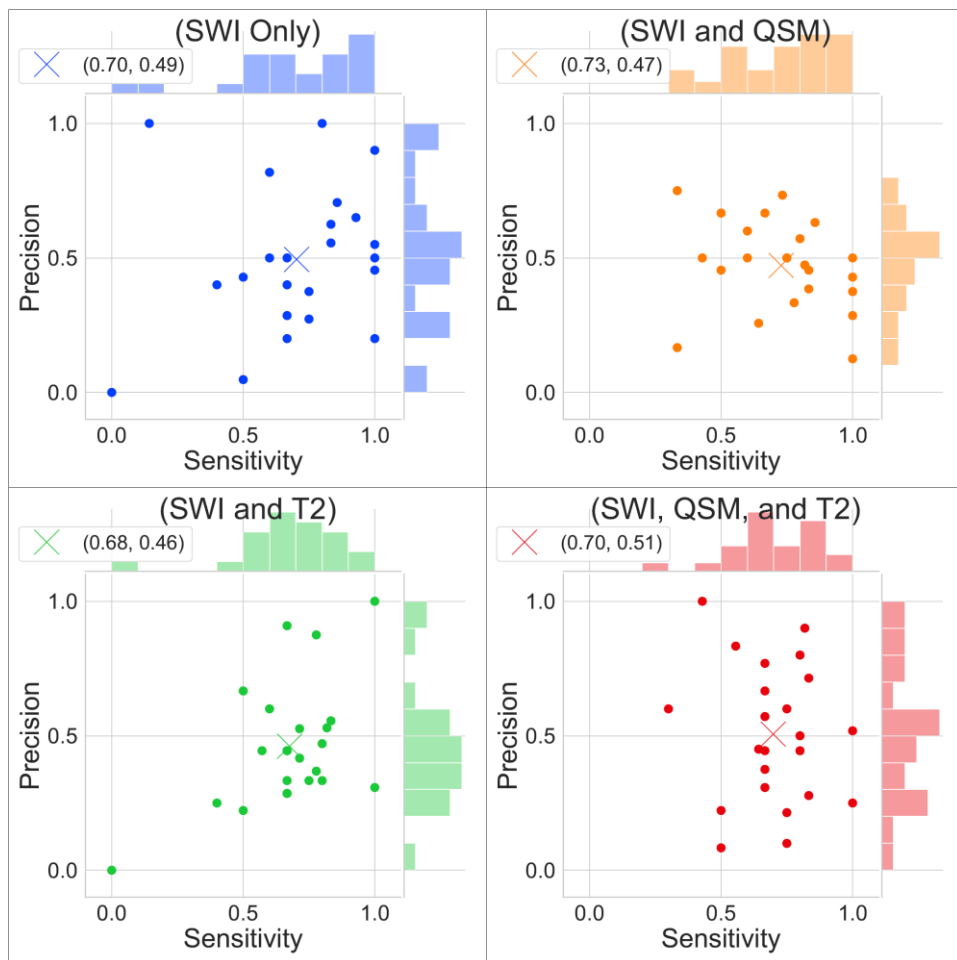
Single Class CMB Only

Single Class Iron Deposits Only

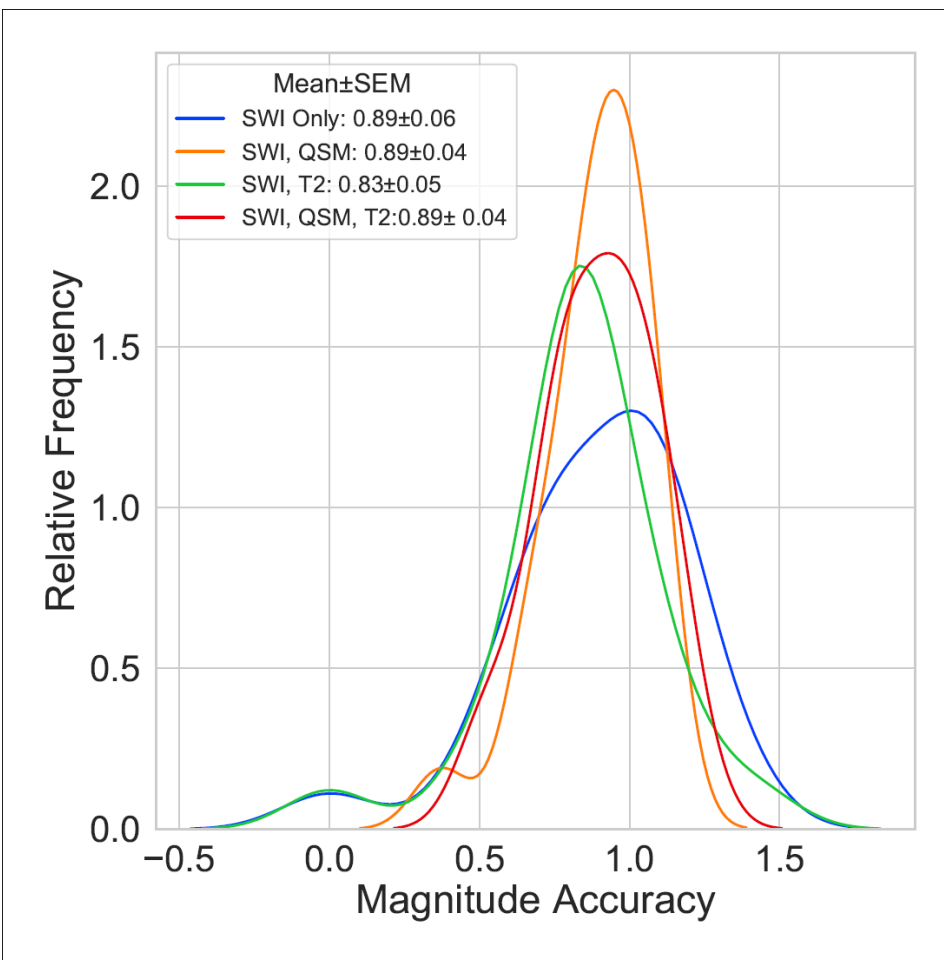


S 5: Joint scatterplots of the sensitivity vs precision of all single class experiments predicting CMBs and non-hemorrhage iron deposits when excluding the outlier participant. (Left) all CMB only experiments and (Right) all iron deposits only experiments. In each subplot, the round points indicate the individual participants' sensitivity and precision evaluated with leave-one-out cross-validation, and the X indicates the mean sensitivity and precision. The legend at the upper left corner of each subplot shows the coordinates of X. In each subplot, histograms of the sensitivity and precision are displayed along the upper and right axes.

Joint Scatterplot for Iron Deposits U CMB



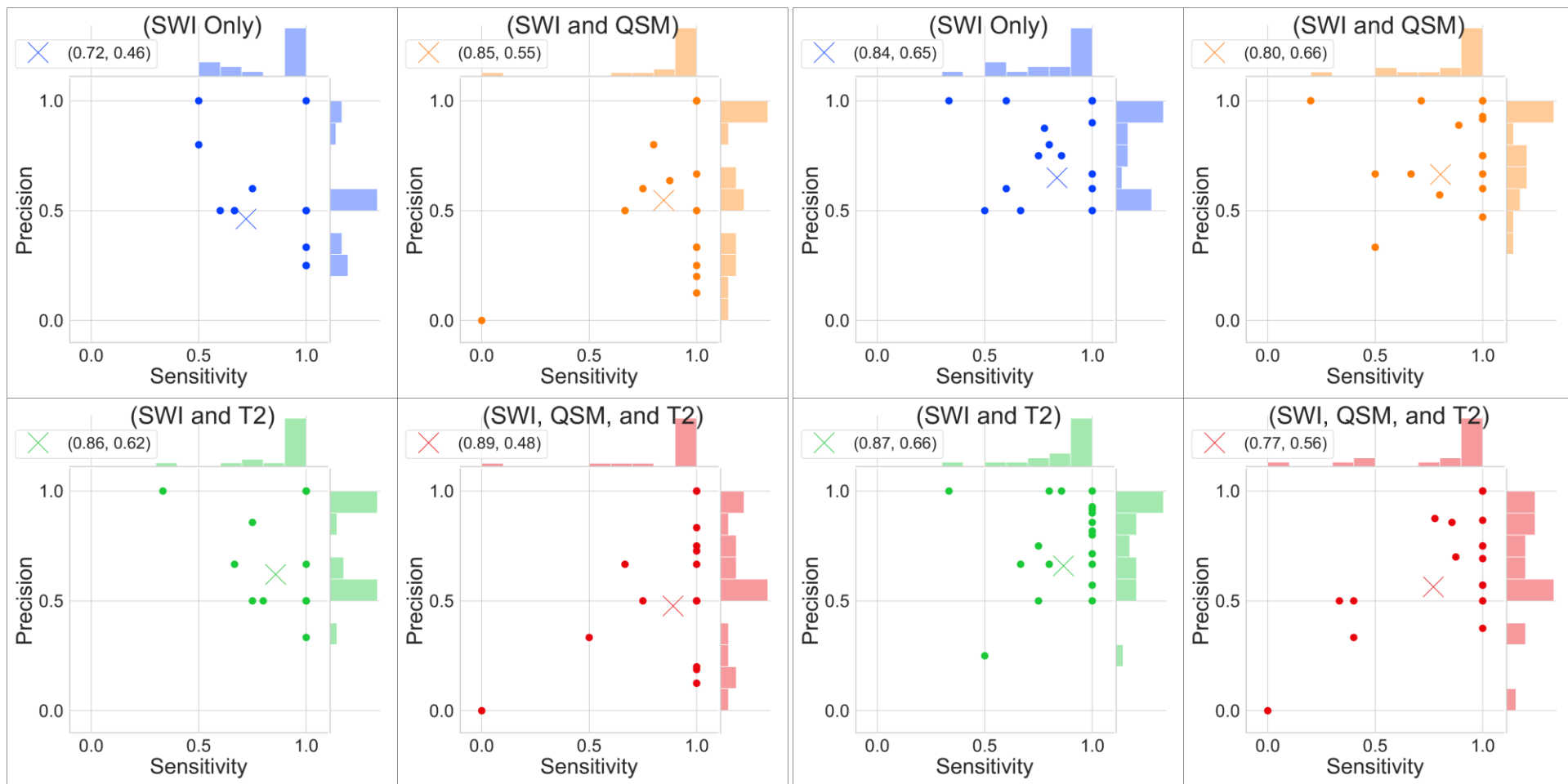
Histogram for Iron Deposits U CMB



S 6: (Left) Joint scatterplots of the sensitivity vs precision for experiments where the combined iron deposit and CMB labels were used and the outlier participant was excluded. In each subplot, the round points indicate the individual participants' sensitivity and precision evaluated with leave-one-out cross-validation, and the X indicates the mean sensitivity and precision. The legend at the upper left corner of each subplot shows the coordinates of X. In each subplot, histograms of the sensitivity and precision are displayed along the upper and right axes. (Right) Histogram of the magnitude accuracy of all single class experiments where the combined iron deposit and CMB labels were evaluated and the outlier participant was excluded. The legends in each subplot indicate the mean magnitude accuracy and standard error of the mean.

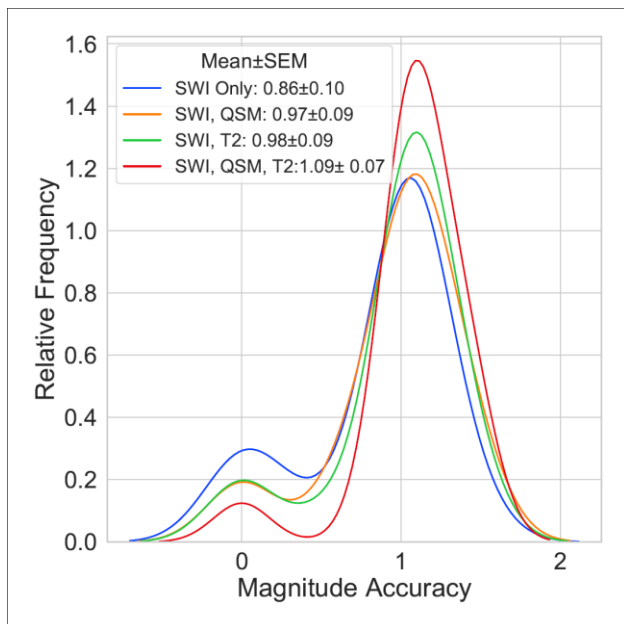
Multiclass CMB

Multiclass Iron Deposits

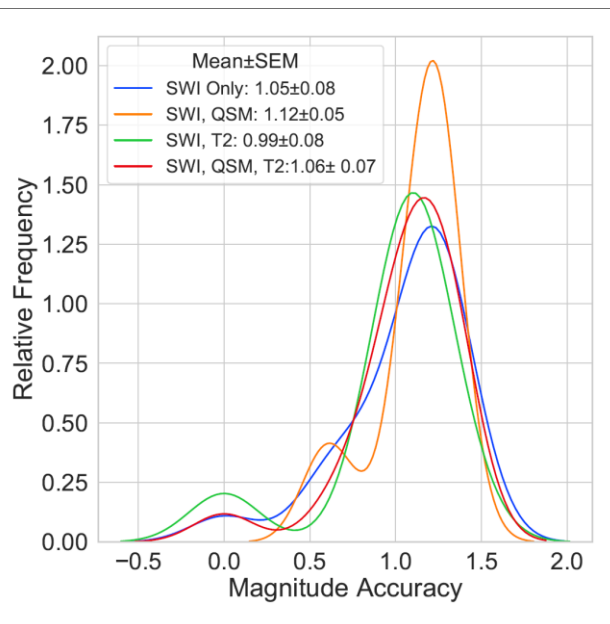


S 7: Joint scatterplots of the sensitivity vs precision of all multiclass experiments predicting CMBs and non-hemorrhage iron deposits when excluding the outlier participant. (Left) all evaluations for CMBs and (Right) all evaluations for iron deposits. In each subplot, the round points indicate the individual participants' sensitivity and precision evaluated with leave-one-out cross-validation, and the X indicates the mean sensitivity and precision. The legend at the upper left corner of each subplot shows the coordinates of X. In each subplot, histograms of the sensitivity and precision are displayed along the upper and right axes.

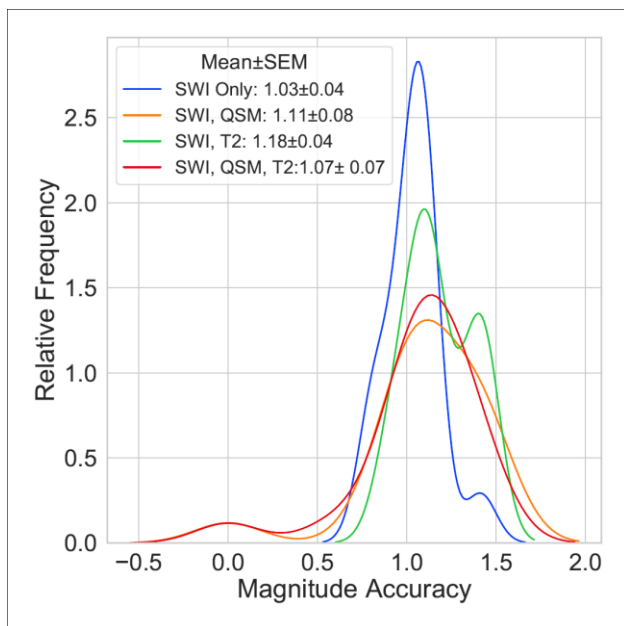
Single Class CMB Only



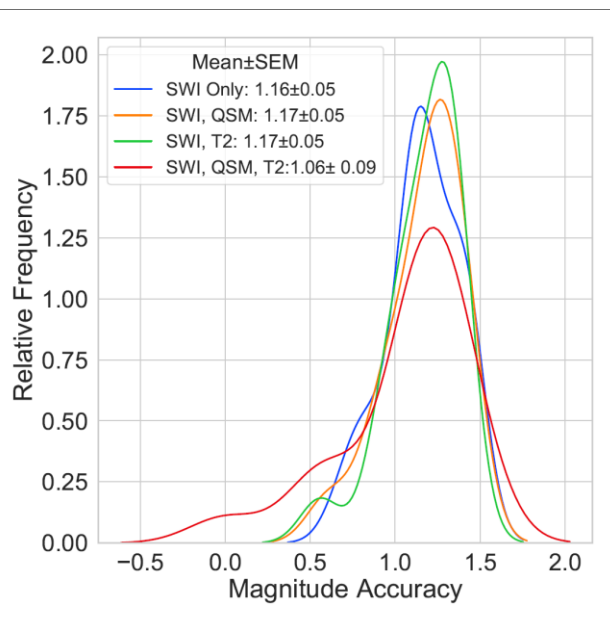
Single Class Iron Deposits Only



Multiclass CMB



Multiclass Iron Deposits



S 8: Histogram of the magnitude accuracy of all single class CMB only and non-hemorrhage iron deposits only experiments (top row) and multiclass CMB and non-hemorrhage iron deposit (bottom row) experiments where the outlier participant was excluded. The legends in each subplot indicate the mean magnitude accuracy and standard error of the mean.

References

1. Gregoire, S., et al., The Microbleed Anatomical Rating Scale (MARS): reliability of a tool to map brain microbleeds. *Neurology*, 2009. 73(21): p. 1759-1766.
2. Cordonnier, C., et al., Improving interrater agreement about brain microbleeds: development of the Brain Observer MicroBleed Scale (BOMBS). *Stroke*, 2009. 40(1): p. 94-99.
3. Ronneberger, O., P. Fischer, and T. Brox. U-net: Convolutional networks for biomedical image segmentation. in *International Conference on Medical image computing and computer-assisted intervention*. 2015. Springer.
4. Van Hulse, J., T.M. Khoshgoftaar, and A. Napolitano. Experimental perspectives on learning from imbalanced data. in *Proceedings of the 24th international conference on Machine learning*. 2007. ACM.
5. Vernooij, M., et al., Prevalence and risk factors of cerebral microbleeds: the Rotterdam Scan Study. *Neurology*, 2008. 70(14): p. 1208-1214.
6. Lee, S.-H., et al., Cerebral microbleeds in patients with hypertensive stroke. *Journal of neurology*, 2004. 251(10): p. 1183-1189.